Bioactive Materials 45 (2025) 257–273

Contents lists available at ScienceDirect

Bioactive Materials

journal homepage: www.keaipublishing.com/en/journals/bioactive-materials

Rapid assessment of the osteogenic capacity of hydroxyapatite/aragonite using a murine tibial periosteal ossification model

Emma Steijvers [a,1], Yunshong Shi [a,b,1], Hong Lu [a,c], Weixin Zhang [d], Yitian Zhang [e], Feihu Zhao [e], Baichuan Wang [a,f], Louise Hughes [g], Jake E. Barralet [h], Giulia Degli-Alessandrini [i], Igor Kraev [i], Richard Johnston [e], Zengwu Shao [f], Frank H. Ebetino [j], James T. Triffitt [k], R. Graham G. Russell [k,l], Davide Deganello [e], Xu Cao [d,**], Zhidao Xia [a,*]

[a] Centre for Nanohealth, Swansea University Medical School, Faculty of Medicine, Health and Life Science, Swansea University, Swansea, United Kingdom
[b] School of Stomatology, Tongji Medical College, Huazhong University of Science and Technology, Wuhan, 430030, China
[c] Department of Orthopaedics, Xiangyang Central Hospital, No. 136, Jingzhou Street, Xiangyang City, Hubei Province, China
[d] Department of Orthopaedics, Johns Hopkins Medical School, Baltimore, MD, 21205, United States
[e] Faculty of Science and Engineering, Swansea University, Swansea, United Kingdom
[f] Department of Orthopaedics, Union Hospital, Tongji Medical College, Huazhong University of Science and Technology, Wuhan, China
[g] Oxford Instruments NanoAnalysis, Halifax Road, High Wycombe, Bucks, HP12 3SE, United Kingdom
[h] Faculty of Dentistry and Health Sciences, Surgical and Interventional Sciences Division, Department of Surgery, Faculty of Medicine and Health Sciences, McGill University, Quebec, Canada
[i] The Open University, Electron Microscopy Suite, Walton Hall, Milton Keynes, MK7 6AA, United Kingdom
[j] Department of Chemistry, University of Rochester, Rochester, NY, 14627, United States
[k] Nuffield Department of Orthopaedics, Rheumatology and Musculoskeletal Science, University of Oxford, Oxford, United Kingdom
[l] The Mellanby Centre for Musculoskeletal Research, Division of Clinical Medicine, School of Medicine and Population Health, University of Sheffield Medical School, Sheffield, S10 2RX, United Kingdom

ARTICLE INFO

Keywords:
Osteogenesis assessment
Intramembranous ossification
Tibial periosteal bone formation
Hydroxyapatite/aragonite
Biomaterials

ABSTRACT

Biomaterials are widely used as orthopaedic implants and bone graft substitutes. We aimed to develop a rapid osteogenic assessment method using a murine tibial periosteal ossification model to evaluate the bone formation/remodelling potential of a biomaterial within 2–4 weeks. A novel hydroxyapatite/aragonite (HAA) biomaterial was implanted into C57BL/6 mice juxtaskeletally between the tibia and tibialis anterior muscle. Rapid intramembranous bone formation was observed at 14 days, with 4- to 8-fold increases in bone thickness and callus volume in comparison with sham-operated animals ($p < 0.0001$), followed by bone remodelling and a new layer of cortical bone formation by 28 days after implantation. The addition of zoledronate, a clinically-utilised bisphosphonate, to HAA, promoted significantly more new bone formation than HAA alone over 28 days ($p < 0.01$). The osteogenic potential of HAA was further confirmed by implanting into a 3.5 mm diameter femoral cancellous bone defect in rats and a 5 mm diameter femoral cortical bone defect in minipigs. To understand the biodegradation and the cellular activity at the cell/biomaterial interfaces, non-decalcified specimens were resin embedded and sections subjected to combined scanning electron microscopy (SEM)/electron backscatter diffraction (EBSD)/energy dispersive X-ray spectrometry (EDS) analysis. We conclude that murine tibial periosteal ossification is a novel method for rapid assessment of the interaction of bioactive materials with osteogenic tissues. This study also highlights that combining calcium carbonate with hydroxyapatite enhances biodegradation and osteogenesis.

Peer review under responsibility of KeAi Communications Co., Ltd.

* Corresponding author. Centre for Nanohealth, Swansea University Medical School, Faculty of Medicine, Health and Life Science, Swansea University, Swansea, SA2 8PP, United Kingdom.
** Corresponding author. Department of Orthopaedics, Johns Hopkins Medical School, Baltimore, MD, 21205, United States.
E-mail addresses: xcao11@jhmi.edu (X. Cao), z.xia@swansea.ac.uk (Z. Xia).
[1] Equal contribution as the first author.

https://doi.org/10.1016/j.bioactmat.2024.11.025
Received 31 July 2024; Received in revised form 18 November 2024; Accepted 18 November 2024

1. Introduction

Bone tissue has a naturally unique ability to repair damage by regeneration [1]. However, this process may become less efficient due to ageing, disease, or when the size of the defects caused by tumour or trauma are beyond the capacity of regeneration (known as critical-sized defects; CSDs) [2]. In cases involving large defects, a scaffold or bone graft is needed to augment tissue regeneration [3–5]. For this purpose, biomaterials are widely used as bone and dental implants in clinical practice [3,6–8]. Preclinical *in vivo* assessments are essential to evaluate these materials for regulatory approval [9–11].

Many experimental animal models used for the assessment of bone regeneration are costly and extremely time-consuming [12]. Current bone formation models can largely be divided into orthotopic models, which consider bone growth at a natural location, and ectopic models, where bone growth is induced at a location where bone does not normally grow [13,14].

Ectopic bone formation models are mainly used to test osteoinductive potential such as the effect of bone morphogenic proteins (BMPs) [13,15]. Intramuscular and subcutaneous implantations are performed over as little as 2 and 3 weeks, respectively, although they are more commonly performed over 4- to 12-week schedules [13,16]. However, in these ectopic models bone growth is not achieved in its natural environment and possibly not by the same cells normally involved in fracture repair. These models are therefore not suitable for testing biomaterials without osteoinductive properties.

Orthotopic bone formation models are very frequently used as to assess repair of fractures in CSDs, in which bone tissues are extensively damaged or lost, and biomaterials, bone grafts or other treatments are applied to promote bone regeneration [14]. Rodents and other small animals may be used [17], but large animals such as sheep, pigs or dogs are more commonly used for these procedures [17,18]. A CSD is generally defined as damage to a bone that will not naturally regenerate in the lifetime of the animal under investigation without surgical intervention or a bone graft [19,20]. A wide variety of CSD models exist, in species ranging from rodents to large animals, employing diverse bone types, including long bones and the calvarium [11,17].

The calvarial bone defect model involves removing a circular area of defined diameter from the calvarium, and subsequently observing bone regeneration [19]. This model is highly reproducible for comparative studies [11]. The size of the defect may be 3–15 mm in small animals (mouse, rat and rabbit), and 10–30 mm in large animals (dog, pig or sheep) [2,21]. However, large animal models require appreciable time for bone regeneration and an 8 mm defect may require up to 12 weeks before final evaluation [21,22].

The segmental long bone defect model involves removal of a segment of a long bone, such as femur, tibia, radius or ulna and subsequent observation of bone regeneration [2]. This procedure may be performed in both large (dog, pig, sheep and goat) and small (mouse, rat and rabbit) animals, with the length of the defects being 2–20 mm in small and 6–40 mm in large animals [2]. Inevitably, the wider the gap between the regenerating bone ends the longer the regeneration times needed to achieve bone union and effective healing.

Osteogenic stem cells have been identified on the periosteal bone surface [23–26]. In small animals, these cells lead to the formation of appreciable amounts of bone tissue within 1–2 weeks after bone injury. A method that makes use of the activation of periosteal stem cells for bone regeneration assessment without requiring appreciable bone damage could speed up biomaterial assessments while retaining the benefits of orthotopic bone formation models. To test this hypothesis, we developed a model in which bone scaffolds are carefully implanted between the tibia and the anterior tibialis muscle in mice, hypothesizing that local osteogenic progenitor cells may be activated on the periosteal surface and at the interface between these orthotopic periosteal and ectopic muscle sites. Differences in callus size or structure could then be quantified to assess the potential osteogenic capacity of biomaterials or any reagents that have the potential to influence bone formation.

A novel 3D-printed hydroxyapatite/aragonite (HAA) biomaterial has been developed recently as a biomimetic bone graft substitute (US Patent: 12011515B2). This biomaterial consists of hydroxyapatite that is formed at physiological temperatures as well as biodegradable calcium carbonate in the form of aragonite [27]. We selected HAA as a scaffold for assessing new bone formation in our periosteal ossification model.

Bisphosphonates are a major class of drugs that are used for clinical treatment of many metabolic bone diseases. Because of their high affinity for bone mineral, they are readily accumulated in bone and are relatively specific inhibitors of osteoclasts; the cells that are directly involved in bone resorption [28]. The two bisphosphonates used in this study, OX14 and zoledronate, are nitrogen-containing bisphosphonates that target farnesyl pyrophosphate synthase (FPPS), resulting in the loss of prenylated proteins in osteoclasts, thereby inhibiting bone resorption [29,30]. It has been reported that by using bisphosphonates to inhibit bone resorption during fracture healing, larger calluses with enhanced mechanical properties can be formed [31–33]. In order to ascertain in the present study whether callus size could be a useful determinant of osteogenic capacity, HAA scaffolds were compared with bisphosphonate-infused HAA scaffolds.

In this study, we report a murine model in which the tested biomaterials were implanted on the surface of the tibia and in contact with the anterior tibialis muscle. The experimental design is shown in Fig. 1. Two bisphosphonates, OX14 and zoledronate, were added to HAA and new bone formation was quantified and compared between treatments. The advantages of this model are: (1) no appreciable bone defects or fracture are induced for the purpose of screening effective materials, therefore minimising animal harm; (2) rapid bone formation within 14 days, followed by bone remodelling within 28 days, so evaluation of bone formation, bone resorption and biomaterial degradation can be performed; (3) appreciable amounts of bone tissue are formed, showing 4–8-fold greater bone formation compared with sham groups, making this method suitable for quantitative analysis and intergroup comparisons; (4) evaluation of both orthotopic and ectopic bone formation are possible as the implants are in direct contact with both bone and muscle; and (5) changes in pharmaceutical composition of the implanted materials can be analysed quantitatively. The effects of biomaterials on osteogenesis were further evaluated in this study by using rats and minipigs, with consistent outcomes being observed. In addition, we report a method for preparing undecalcified bone/biomaterial samples for ultrastructural as well as compositional analysis.

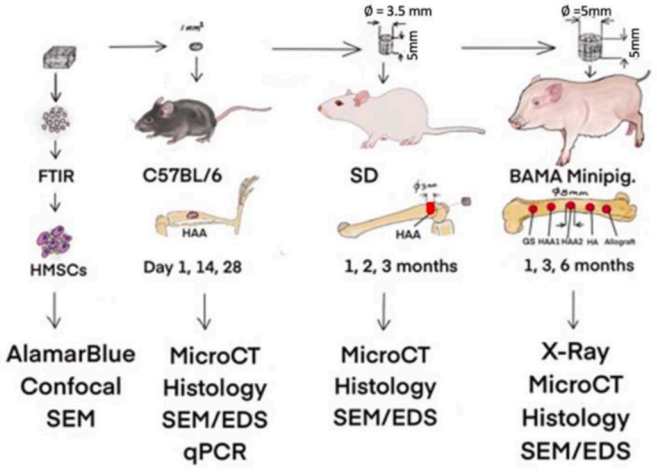

Fig. 1. Design of *in vitro* and *in vivo* tests.

2. Materials and methods

2.1. Biomaterial preparation and characterisation

Hydroxyapatite/aragonite (HAA) was prepared as previously described [27]. Briefly, tetracalcium phosphate (TTCP, Matexcel, Shirley, NY, USA) and $CaHPO_4$ (Sigma-Aldrich St Louis, MO, USA) were combined in a 1:1 M ratio, and $CaCO_3$ (Sigma-Aldrich) was added before mixing thoroughly using a mortar and pestle. Ten grammes of the combined powders were then mixed with 5 g carrier liquid consisting of a gelatine solution in water. The paste was then either printed using a 3D-Bioplotter® (Envisiontec GmbH, Gladbeck, Germany) [27], or moulded and left to dry at room temperature. The scaffolds were crosslinked in 0.1 % glutaraldehyde (Sigma-Aldrich) and soaked in PBS (Gibco, Carlsbad, CA, USA) at 37 °C for 24 h before being air dried in a 37 °C oven. The materials were autoclaved before *in vitro* or *in vivo* assessment.

The ratio of $CaCO_3$ in HAA was 40 % weight/weight. For the study using minipigs, an additional group (HAA1) was tested in which the ratio of $CaCO_3$ was 20 % weight/weight.

For FTIR analysis, HAA scaffolds were soaked in PBS for 0 and 24 h. In two groups the HAA was mixed with either 1.6 μg of zoledronate or 7.5 μg of OX14 per mg of scaffold dry weight to observe the effect of bisphosphonate on hydroxyapatite crystallisation before being soaked in PBS/bisphosphonate (OX14 and zoledronate) for 24 h. The concentration of zoledronate and OX14 was determined based on a previous publication [29]. All scaffolds were air-dried and subsequently powdered. FTIR analysis was then performed on the samples using a Perkin Elmer Spectrum 100 FTIR spectrophotometer (Perkin Elmer, Waltham, MA, USA).

2.2. In vitro assessments

2.2.1. Human umbilical cord mesenchymal stem cell (hUCMSC) isolation

Human umbilical cords were sourced from Singleton Hospital, Swansea, and were taken only with fully informed consent of the anonymised donors (West Wales Research Ethics Committee REC11/WA/0040). The isolation, culture conditions and characterisation were as reported previously [34]. In Brief, hUCMSCs were isolated via explant culture and maintained in DMEM/F12 supplemented with 10 % foetal bovine serum (FBS) and 1 % penicillin/streptomycin (Gibco).

2.2.2. Cell viability assay

For cell viability assays, HAA granules with a diameter of 300–400 μm (0.017 ± 0.002 g) were added to 31,250, 61,250, 12,5000, 250,000 or 500,000 hUCMSCs and seeded into 35 mm culture dishes. Alamar Blue assays and confocal fluorescence microscopy were performed at 3, 7, 14 and 21 days after seeding as described previously [34].

2.2.3. Osteogenic differentiation

The *in vitro* osteogenic capacity of hUCMSCs was assessed via alkaline phosphatase (ALP) quantification and ALP/alizarin red S staining following differentiation (Supplementary methods) in osteogenic medium containing 50 μg/ml L-ascorbic acid, 10 mM β-glycerophosphate and 1 μM dexamethasone (Sigma-Aldrich). The samples were assessed at day 7, 14 and 21 following induction of osteogenic differentiation as described previously [34].

2.3. Assessment of periosteal osteogenesis of HAA in mice

2.3.1. Material preparation

Approximately 1.5 mg of HAA granules (approximately 1 mm^3 in volume) were divided into three groups, and soaked in either 2.45 μg/mL zoledronate in PBS, 11.35 μg/mL OX14 in PBS, or PBS only for 90 min, then air-dried at 37 °C overnight.

2.3.2. Implantation juxtaskeletally between the tibia and the tibialis anterior muscle in mice

To compare the effects on patterns of osteogenesis among the sham operation group and those with surgical implantation of HAA, HAA-OX14, and HAA-zoledronate, a total of 54C57BL/6 wild-type (wt) mice were used for this study. All experiments were performed at Johns Hopkins University, Baltimore, MD, USA and were performed in accordance with local and university regulations. The animal protocols were approved by the Institutional Animal Care and Use Committee of Johns Hopkins University (MO21M276). Three-month-old C57BL/6 (wt) mice, obtained from the Jackson Laboratory (strain number: 000664), were anaesthetised using 0.18–0.25 mL of anaesthetic [13 mg/mL ketamine hydrochloride (Ketalar) and 1.2 ng/mL Xylozine (Sigma-Aldrich) in PBS (Corning)].

One scaffold piece was implanted into each hindlimb, between the tibia and anterior tibialis muscle. The mice were divided into four groups as shown in Table 1. After 1, 14 or 28 days the mice were killed using FORANE gas (isoflurane USP, Baxter International Inc., Deerfield, IL, USA). The right limbs were removed, immediately frozen in liquid nitrogen for PCR analysis, and the left limbs were fixed in 10 % formalin (Thermo Fisher Scientific, Waltham, MA, USA) for micro computed tomography (microCT) analysis and histology (Table 1).

2.3.3. qPCR analysis

The right limbs from five mice in each group were homogenized using a sonifier and RNA was isolated from the tissue using a QIAGEN RNeasy mini kit (Qiagen, Valencia, CA, USA). Reverse transcription was initiated by adding PrimeScript RT Mastermix (TaKaRa Bio Inc., Shiga, Japan) to the RNA and incubating the tubes at 37 °C for 15 min, then at 85 °C for 5 s before cooling. The cDNA, along with water and primers, was added to SYBR green PCR Master Mix (Qiagen) and the reaction was run for 40 cycles. A list of the primers used, and their sequences is given in Table 2.

2.3.4. MicroCT analysis

Left limbs were scanned using a Skyscan X-ray microtomography system (Bruker MicroCT, Kontich, Belgium) at a voltage of 65 kV and current of 153 μA. A pixel size of 6, rotation of 0.3 and high-resolution exposure time of 218 ms were used for scanning.

Due to the special feature of biomaterial implantation on the surface of the tibial bone, the normal microCT quantitative analysis did not segment the biomaterial and bone region automatically. Therefore, a manual segment analysis was performed by using the "ROI-drawing" function in the cTAN software. Subsequently by using the "3D Analysis" function in the same software, the volume of bone tissue and biomaterial (in cubic millimetres) could be quantified and compared.

2.3.5. Gross appearance, SEM-EDS and histology

Mouse tibial specimens were embedded in LR Gold resin (Agar Scientific) with 1 % w/v benzoyl peroxide (Agar Scientific Ltd. Stansted, UK) following the manufacturer's protocol. After curing, the samples were polished to expose the implant/tibia interface and initially grossly imaged using a TM-DM10 imaging system (Tomlov, HUIRUI Investment Management Ltd, Hubei, China).

Table 1
Experimental animal groups.

Groups	Material	Preparation	Tibia (left)	Tibia (right)
Group 1	Sham	n/a	4 % formaldehyde in PBS, followed by microCT, resin embedding, sectioning, and histology	RNA extraction, cDNA, qPCR for gene expression
Group 2	HAA	Soaked in PBS		
Group 3	OX14 + HAA	Soaked in 11.35 μg/mL		
Group 4	Zol + HAA	Soaked in 2.45 μg/mL		

Table 2
Primer sequences used for qPCR analysis.

Linked to	Gene	Forward (5′ to 3′)	Reverse (5′ to 3′)
Housekeeping	GAPDH	CATCACTGCCACCCAGAAGACTG	ATGCCAGTGAGCTTCCCGTTCAG
Osteoblast activity	TGFβ	CCACCTGCAAGACCATCGAC	CTGGCGAGCCTTAGTTTGGAC
	BMP2	GGGACCCGCTGTCTTCTAGT	TCAACTCAAATTCGCTGAGGAC
Osteoblast differentiation	Osterix	ATGGCGTCCTCTCTGCTTG	TGAAAGGTCAGCGTATGGCTT
	Osteocalcin	CAGACACCATGAGGACCATC	GGACTGAGGCTCTGTGAGGT
	Col1a1	GCTCCTCTTAGGGGCCACT	CCACGTCTCACCATTGGGG
Osteoclast differentiation	CSFR	GTGTCAGAACACTGTAGCCAC	TCAAAGGCAATCTGGCATGAAG
	CSK	CCGAGCGGCTTCTTTACCC	GCATGATACATGATGCGGTAGT
Osteoclast fusion	CCR2	ATCCACGGCATACTATCAACATC	TCGTAGTCATACGGTGTGGTG
	OCSTAMP	CTGTAACGAACTACTGACCCAGC	CCAGGCTTAGGAAGACGAAGA
	CD47	TGGTGGGAAACTACACTTGCG	CGTGCGGTTTTTCAGCTCTAT
	OSTM1	GAGCTGACCGCCTGTATGG	ATGTTTCGGCTGATGTTGTCC
Nerve markers	Netrin1	CAGCCTGATCCTTGCTCGG	GCGGGTTATTGAGGTCGGTG
	CGRP	CAGTGCCTTTGAGGTCAATCT	CCAGCAGGCGAACTTCTTCTT
	PGP9.5	AGGGACAGGAAGTTAGCCCTA	AGCTTCTCCGTTTCAGACAGA
Netrin1 receptor	DCC	CAAGCTGGCTTTTGTACTCTTCG	GAACTCCTCGGTCGGACTCT
Vascularization	Pdgfbb	CATCCGCTCCTTTGATGATCTT	GTGCTCGGGTCATGTTCAAGT
	Angiogenin	CCAGGCCCGTTGTTCTTGAT	GCAAACCATTCTCACAGGCAATA

The samples were spark-coated with carbon and imaged using a TESCAN CLARA SEM equipped with a retractable in-chamber backscatter electron (BSE) detector and with an energy dispersive spectroscopy (EDS) detector (Oxford Instruments Ultim Max with 170 mm^2 sensor; Oxford Instruments, Abingdon, UK) for compositional analysis of the elements Ca, P, C, N, and O.

After SEM analysis, the same samples were sectioned without decalcification using a laser microtome (LLS ROWIAK LaserLabSolutions GmbH, Hannover, Germany). Sections at 10 μm thickness were stained with Mason–Goldner trichrome and toluidine blue (Supplementary methods) and imaged using a Zeiss light microscope (Carl Zeiss Microscopy GmbH, Jena, Germany).

2.4. Assessment of in vivo femoral intercondylar trabecular bone defect regeneration in rats

2.4.1. Femoral intercondylar 3.5 mm diameter trabecular bone defects

To confirm the effect of HAA on osteogenesis in bone defects in comparison with gelatine sponge, eighteen Sprague–Dawley (SD) rats, each weighing 250 g, were used and all procedures were performed with the approval of the Institutional Animal Care and Use Committee of Tongji Medical School, Huazhong University of Science and Technology, China (IACUC Number 738).

Bone defects were created in the intercondylar region of the femur and HAA or gelatine sponge was implanted into the defect as shown in Table 3.

The rats were anaesthetised by intravenous injection of chloral hydrate according to the protocol approved at the time [35] and since proven to be an excellent intravenous anaesthetic for surgical manipulations in rats [35]. An intercondylar bone defect 5 mm × 3.5 mm diameter was created in the distal femur of each left hind leg. The rats were divided into two groups, control (gelatine sponge) and HAA.

Analgesia was achieved using ketoprofen (Arshine Pharmaceutical Co., Limited, Hunan, China) 5 mg/kg, which was subcutaneously injected once daily for two days following the operative procedures. At 1, 2 and 3 months after operation, the rats were euthanized and the left distal femurs containing the implants were harvested and fixed immediately in neutral 10 % formalin.

Table 3
Experimental design of implant surgery.

Implant	1 month	2 months	3 months
HAA	3	3	3
Control (gelatine sponge)	3	3	3

2.4.2. MicroCT

The fixed samples were used for MicroCT (Scanco VivaCT40; Scanco Medical AG, Bassersdorf, Switzerland) using 70 kV voltage, 21 μm layer thickness and 200 ms scanning speed.

2.4.3. Sample preparation for histology and SEM

After micro-CT scanning, the samples were sawn into two halves to reveal the area of interest and also facilitate orientation. Following serial dehydration, samples were embedded in L R White resin (London Resin Company, Reading, UK) and undecalcified sections were produced for toluidine blue staining.

2.5. SEM/EBSD/EDS observation

After histological sectioning, the tissue blocks were polished and observed using ZEISS EVO LS25 for SEM/EBSD/EDS analysis. Captured images of all the samples were analysed using ImageJ (NIH, Bethesda, MD).

2.6. Assessment of in vivo femoral cortical bone defect regeneration in BAMA minipigs

2.6.1. Minipig femoral cortical bone defects

To test the osteogenic potential of HAA, or of HAA1, which contained one-half the calcium carbonate content of the HAA, in cortical bone defects, 15 adult male BAMA minipigs, with a body weight between 30 and 35 kg, were used in the study. The minipigs were anaesthetised by intramuscular injection of Zoletil at 20 mg/kg. A 10 cm incision was created between the large trochanter and the lateral femoral condyle. Five bone defects with a diameter of 5 mm were created in the outer cortex of the bone, with a depth extending from the surface of the bone cortex to the medullary cavity, but not penetrating the medial cortex.

To compare the effect of HAA and HAA1 with control and commercially available bone graft materials, each femur was implanted with five materials for parallel comparison (Fig. 9A and B): 1) Control (gelatine sponge GS); 2) HAA1; 3) HAA; 4) HA (hydroxyapatite cement, Shanghai Rebone Biomaterias Co. Ltd., Shanghai, China); 5) pig demineralised bone matrix (pDBM; Jin Gu Wei, Shanghai Qiaobo Science and Technology Development Ltd, Shanghai, China).

2.6.2. Sample preparation

After implantation, the minipigs were killed at 1 day, 1 month, 3 months and 6 months. The whole femur with the five implanted samples was harvested and fixed in 10 % neutral formaldehyde. The specimens were then examined using X-Ray radiography then further fixed in 70 % ethanol.

2.6.3. Undecalcified sections and toluidine blue staining

The samples were dehydrated and embedded in L R White resin using the same procedure as described for the rat samples. The undecalcified samples were sectioned at 100 μm thickness using a Leica SP1600 saw microtome (Leica, Nuddeloch, Germany) and further polished before being stained with toluidine blue and observed under a Zeiss light microscope.

2.6.4. Scanning electron microscopy

A 100 μm section from each sample was collected, polished, then surface stained with uranium acetate and lead citrate before being observed under a TESCAN Mira-3 SEM/EBSD with element analysis using an X-MaxN 80 (Oxford Instruments) and a TESCAN-S8000 SEM/EBSD and an Ultrim Extreme EDS system (Oxford Instruments).

Selected samples were further examined under a TESCAN-S8000 SEM using BSE and a windowless Ultim Extreme EDS detector (Oxford Instruments).

2.7. Statistical analysis

All data are presented as mean ± standard deviation. T-tests were used when comparing two groups whereas one-way analysis of variance (ANOVA) was performed for comparison of multiple groups using GraphPad Prism software. A p-value <0.05 was considered statistically significant.

3. Results

3.1. HAA biomaterial characterisation

The material preparation and FTIR analysis are shown in Fig. 2A and B respectively. FTIR analysis of the individual components revealed distinct peaks for TTCP and HA, exhibiting a jagged or smooth profile around a 1050 nm wavelength. FTIR analysis confirmed that HA conversion was maintained after PBS soaking, with no significant impact being observed with prolonged soaking beyond 24 h. Notably, the addition of bisphosphonates to the scaffold prior to the conversion process was found to impede HA formation (Fig. 2B).

Soaking HAA in PBS is an important step for HAA crystallisation, as confirmed by SEM observations (Supplementary Fig. 1A and B), which align with the findings from FTIR analysis.

3.2. In vitro assessments of viability and osteogenic differentiation

The HAA scaffold granules, when seeded with hUCMSCs, formed nodules/organoid-like structures within 7 days (Fig. 3A, Supplementary Fig. 1C and D). Alamar Blue assays at 3, 7, 14 and 21 days showed that hUCMSCs seeded on HAA at different densities increased in number, thereby confirming that HAA is a non-cytotoxic material that supports this cell growth *in vitro*. However, cell numbers reached a plateau when surface space became limited (Fig. 3B).

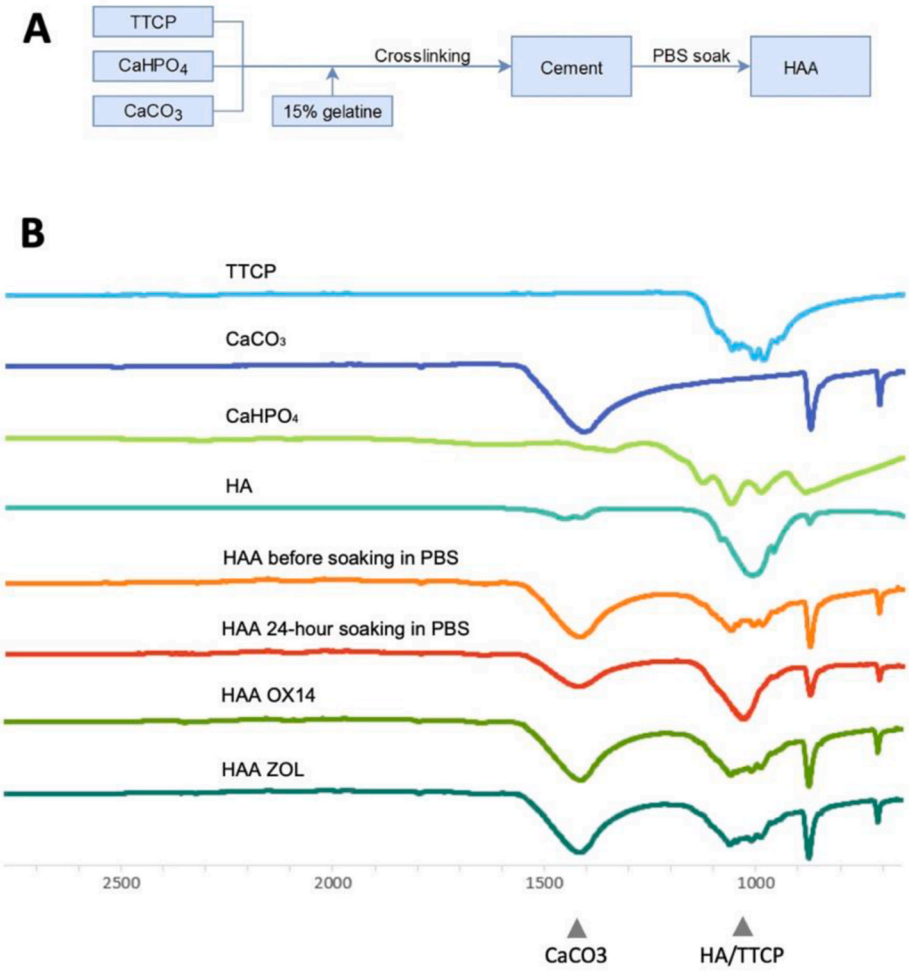

Fig. 2. Material synthesis and characterisation. A. The material preparation of HAA. **B.** FTIR characterisation of the raw materials and the end products at different stages of the HAA fabrication processes. The mixing of the raw materials to form a cement is the first step where the crystallisation of hydroxyapatite requires soaking the cement in PBS for a minimum time of 24 h. Adding bisphosphonate OX14 or zoledronate caused deficient HA crystallisation. Typical peaks for $CaCO_3$ are 712, 874 and 1418 cm^{-1}. The peak of phosphate in hydroxyapatite is at 1100 cm^{-1}.

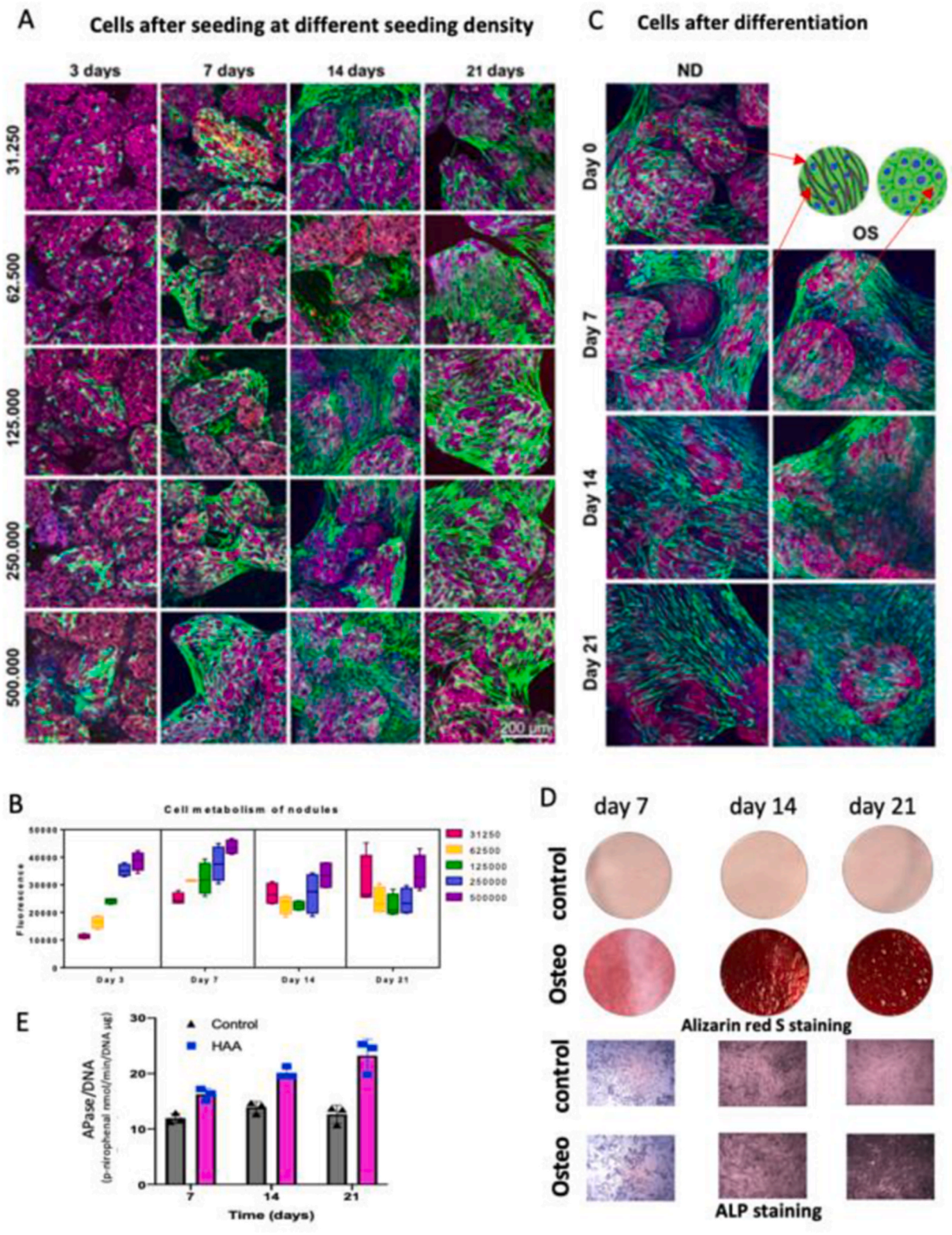

Fig. 3. Assessment of hUCMSC proliferation and differentiation on HAA *in vitro*. A. Confocal microimages of hUCMSCs at different seeding densities on HAA over 21 days. **B.** Alamar Blue assay of cell metabolism of cultures shown in A. At different seeding densities, hUCMSC numbers peaked at day 7 and plateaued after 14 days. **C.** hUCMSCs cultured in control or osteogenic differentiation medium on HAA demonstrated distinct morphologic changes (abstracted in top right panel). **D** The differentiation potential of hUCMSCs in control and osteogenic media over 21 days, illustrated by alizarin red S and alkaline phosphatase staining. **E.** Quantitative analysis of alkaline phosphatase normalised to DNA content of hUCMSCs on HAA over 21 days.

MSCs cultured in osteogenic differentiation medium demonstrated distinct morphological changes (Fig. 3C). The osteogenic potential of hUMCSCs was confirmed by alkaline phosphatase (ALP) and alizarin red S staining (Fig. 3D) and ALP quantitative analysis (Fig. 3E).

3.3. Assessment of tibial periosteal osteogenesis induced by HAA in mice

3.3.1. The animal model

All 54 mice were observed to move around freely immediately after recovery from anaesthesia. The wound was dry and healed within a week with no infection observed. No analgesia was necessary following careful distress evaluation.

3.3.2. Gross and colour SEM/backscatter/EDS observation of tibial callus formation

One day post-implantation callus formation was not visible in any group. The sham-operated control group showed only minimal callus formation on day 14 post-surgery. In contrast, appreciable callus formation was observed in all experimental groups from day 14 onwards (Supplementary Figure 2 A). The callus formation was confirmed by SEM-EDS for elemental analysis, showing the presence of both calcium and phosphate in the scaffolds, cortical bone and bone calluses (Supplementary Figure 2 B).

In addition, a noteworthy transformation in bone callus morphology was observed between 14 days and 28 days post-implantation. At day 14, the callus consisted of newly-formed trabecular bone; however, by day 28 the callus had undergone significant remodelling, now featuring distinct double cortical layers and a bone marrow cavity between the old and new cortical bone (Supplementary Fig. 2).

3.3.3. MicroCT quantitative analysis

The size and quality of the newly-formed bone calluses was compared through 3D analysis of the microCT scanning data (Fig. 4B).

For microCT analysis, a manual segmentation method was used to extract the boundary of the region of interest (ROI, Fig. 4C), such as the thickness of tibial bone under HAA (orange), the volume of HAA biomaterials (blue region), the new trabecular callus (green) and the new cortical bone (red). The results showed that the volume of implanted HAA materials remained stable over 28 days, with no difference between the groups ($p > 0.05$, Fig. 4D). The thickness of the tibial shaft under the implants increased four-to eight-fold in all three treatment groups in comparison with sham controls at both 14 and 28 days ($p < 0.05$–0.0001, Fig. 4E). The volume of newly-formed trabecular bone callus was more pronounced at day 14, but reduced at day 28 (Fig. 4F), with no differences between the three treatment groups. The new layer of cortical bone only appeared at day 28 after callus remodelling. There was more new cortical bone in the ZOL-treated HAA group than in the other groups ($p < 0.001$, Fig. 4G). The overall new bone formation (trabecular and cortical bone) was also higher in the ZOL-treated HAA group ($p < 0.01$, Fig. 4H).

3.3.4. qPCR

The gene expression after sham and HAA implantation over 28 days is shown as heat maps where blue indicates down-regulation and red up-regulation of the expression of particular genes in comparison with the sham group (Fig. 5). Missing data are shown as an ‘x’.

The genes were selected to represent (1) bone formation (TGFB1, BMP-2, OSX, OCN, Col1a1); (2) bone resorption (CSFR, CSK, CCR2, OCStamp, CD47, OSTM1; (3) nerve innervation (Netrin1, CGRP, PGP9.5, DCC), and (4) angiogenesis (Pdgfbb, Angiogenin).

At day 1 after implantation, osteoblast marker (Ob) expression increased in the HAA, OX14 and Zol groups, while expression of osteoclast markers, apart from CSK, was reduced in all three groups (Fig. 5A). At day 14 after implantation, there were minor increases in the expression of both bone formation and bone resorption marker genes and reduced/stable expression of innervation and angiogenic gene markers in the HAA group compared with the control group. In contrast, in the OX14-and Zol-treated groups, bone formation, resorption and innervation marker expression remained high (Fig. 5B). At day 28 after implantation, gene expression of bone resorption, innervation and angiogenesis markers were all down-regulated in the HAA group compared with the control group. However, bone formation markers were still expressed in both the OX14 and Zol groups, while there was also some upregulation of both innervation and angiogenesis markers in the Zol group (Fig. 5C).

3.3.5. Histology and histochemistry

Masson-Goldner trichrome histological staining and tartrate-resistant acid phosphatase (TRAP) staining of tissue after HAA implantation are shown in Fig. 6. With Masson-Goldner Trichrome staining, mineralized bone matrix is stained green, osteoid and cells red, and cell nuclei blue. At day 1 after HAA implantation, HAA was in contact with the tibia (Fig. 6A). At day 14, new bone formation was observed in the group with HAA implants (Fig. 6B). There was a small amount of bone formation on the surface of the tibia in the sham group at 14 days (Fig. 6C), while in both OX14 and ZOL groups, large callus formation was observed between the HAA and the tibia, with almost a four-fold increase in tibial thickness (Fig. 6D). Intramembranous ossification between the tibia and implanted HAA was shown to be the dominant type of osteogenesis as no endochondral ossification was observed (Fig. 6E). There was also new bone directly deposited onto HAA particles (Fig. 6F). At day 28 in the ZOL group, a layer of new cortical bone was formed on the surface of the callus to form double cortical bone on the tibia (Fig. 6G). New blood vessels had invaded the HAA implants, where osteoblasts directly deposited osteoid and calcified bone matrix onto the surface of HAA (Fig. 6H). A more detailed image of the interface between the HAA and bone tissue is presented at high magnification in Fig. 6I.

All new bone formation was observed between the implants and the tibia at an orthotopic site, with no bone formation being observed between HAA and muscle. Hence, over the time period studied, no detectable ectopic bone tissue formation was induced within muscle tissue.

ACP histochemical staining of HAA implants is shown in Fig. 6K and L. ACP-positive cells surrounded the HAA implants (Fig. 6K), whereas TRAP-positive osteoclasts were mainly present near the new bone surfaces (Fig. 6L).

3.4. Assessment of in vivo bone regeneration in a rat femoral intercondylar trabecular defect

Gross observation showed that the bone defects did not heal over 3 months in the control group (Fig. 7B–D); however, HAA implants supported the skeletal structure with bone regeneration (Fig. 7E–G). The results were confirmed by microCT scans in control (Fig. 7H–J) and HAA implants (Fig. 7K–M) at 3 months after implantation.

The osteogenesis and biodegradation of HAA after implantation was further observed by SEM/backscatter, in which the HAA implants were detectable as high electric density particles, whereas bone appeared as a grey, unified tissue (Fig. 7N, O, and P). There was a gap between bone and HAA at 1 month (Fig. 7N) but the gap was filled with new bone while the HAA material was degraded to give space for new bone formation at 2 months (Fig. 7O). At 3 months most HAA implants were degraded while new bone was formed and fully integrated into the HAA implants (Fig. 7P).

EDS element analysis showed the implants were a mixture of calcium and phosphate, with a high calcium (Ca) and calcium/phosphate ratio (Ca/P) in the HAA implants (Fig. 7Q and R). ImageJ was used to analyse the surface area of the HAA implants in the tissues, and EDS analysis showed significant decreases in area over the three-month period, which is a sign of biodegradation (Fig. 7S).

Fig. 8 shows light microscopic images of non-decalcified sections

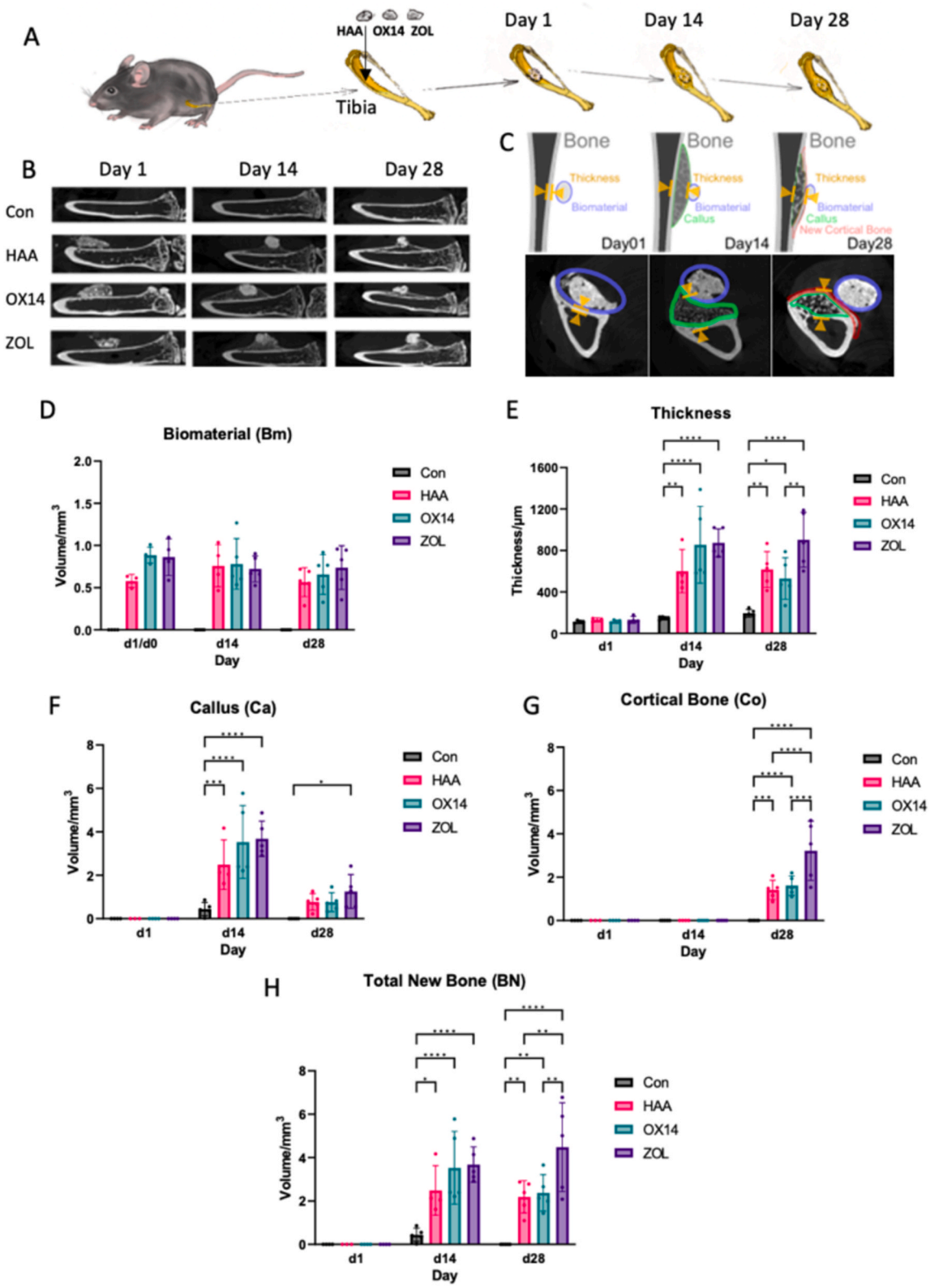

Fig. 4. Assessment of rapid osteogenesis in the mouse tibial periosteal bone formation model. A. Control (Con), HAA, HAA + OX14 (OX14) and HAA + ZOL (ZOL) were implanted on the surface of the tibia and evaluated after 28 days. **B.** microCT cross sections showing HAA-conductive periosteal bone formation on the tibia in all groups. **C.** Manual segmentation of total volume of implants, bone thickness, callus, new cortical bone and total new bone volume of HAA-conductive osteogenesis. **D.** There was no difference in the total volume of implants at 28 days, implying no significant biodegradation over 28 days. **E.** Significant increases in bone thickness were observed in all three groups with HAA implantation at 14 and 28 days compared with the sham group. **F.** Significantly greater volumes of callus formation were observed in all three groups with HAA implantation at 14 days, compared to the sham control group. **G.** Significantly greater volumes of new cortical bone formation were observed on the surface of the callus in all three groups with HAA implantation compared to controls; however the ZOL group showed more cortical bone formation than either the HAA or OX14 groups ($p < 0.01$). **H.** All three groups with HAA implantation showed increased volumes of new bone formation compared with the sham group, whereas the ZOL group showed more new bone formation than the HAA or OX14 groups ($p < 0.01$).

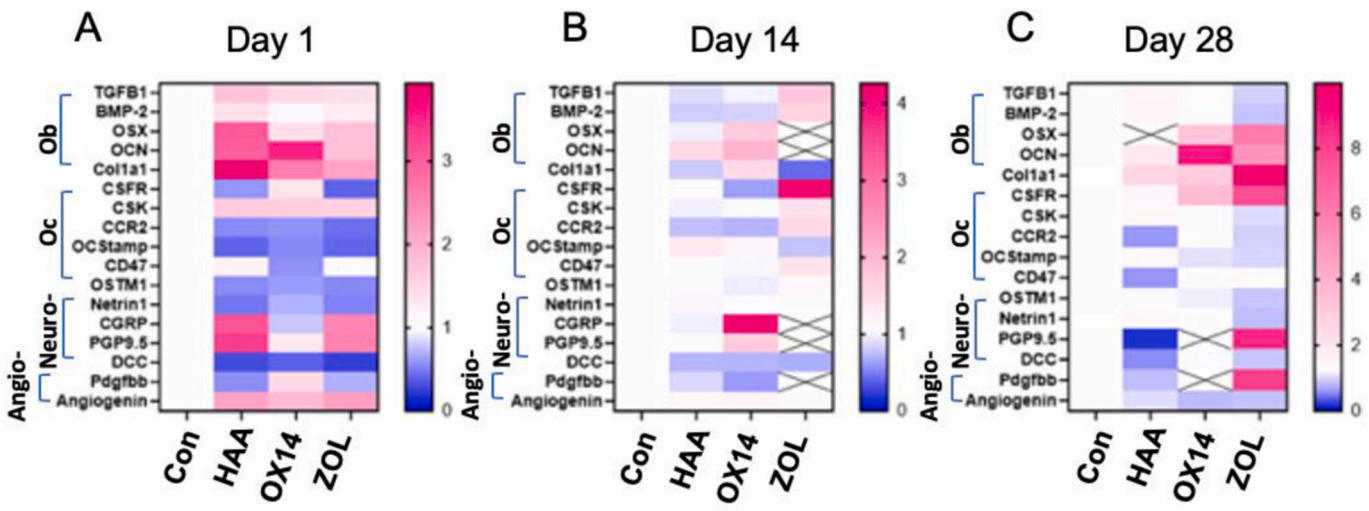

Fig. 5. Heatmaps showing qPCR analysis of biomarkers in tissue after HAA implantation. Gene expression of various marker genes is shown as the fold change compared to the Sham control. Each field represents a pool of samples (N = 4–5) averaged over two technical replicates. Downregulation is indicated by a blue colour, while overexpression is indicated in pink. Missing results are shown as crossed out fields. **A.** Day 1 after implantation. **B.** Day 14 after implantation. **C.** Day 28 after implantation.

stained with toluidine blue after implantation of HAA or control (gelatine sponge) implants into a 3.5 mm femoral intercondylar defect. In the control group with gelatine sponge implantation over 3 months, only fibrous tissue was observed without any bone formation (Fig. 8A). At 1 month after HAA implantation, fibrous tissue could be seen infiltrating into the implants (Fig. 8B). At 2 months after HAA implantation, bone formation was apparent on the surface of the HAA (Fig. 8C), and new blood vessels were infiltrating into the core of the HAA implants (Fig. 8D).

In a typical region of osteogenesis on HAA at 3 months, osteoclasts were visible, removing the implants, which was followed by bone formation by osteoblasts (Fig. 8E). At the interface between bone and HAA, osteoblasts could be seen on both bone and HAA surfaces (Fig. 8F). At high magnification (Fig. 8E), active bone formation by osteoblasts was visible, with osteocytes embedded within the bone matrix (Fig. 8G) at the frontier of HAA. Fig. 8H shows the implanted HAA being resorbed by two typical multinucleated osteoclasts with ruffled borders.

3.5. HAA enhances in vivo femoral cortical bone defect regeneration in BAMA minipigs

The bone graft materials: gelatine sponge (GS); HAA1; HAA; HA, and pDBM were harvested at 1 day, 1 month, 3 months and 6 months after implantation (Fig. 9A and B) and analysed by X-ray, toluidine blue staining and SEM/backscatter Fig. 9). After GS implantation, the bone defects were only partially healed even at 6 months (Fig. 9G5 and G8). In contrast, in the HAA1, HAA and pDBM groups, full healing of the bone defects was achieved (Fig. 9H5–I5, Fig. 9H8–I8 and Fig. 9K5–K8). In pure HA implants, even though bone growth was apparent on the material, clear boundaries and gaps remained visible at the interface between the bone and the implants (Fig. 9J5 and J8).

SEM/backscatter observation of the interfaces between the implants (HAA1, HAA and HA) and bone are shown at 1, 3 and 6 months (Fig. 10). The overall surface structure of each group at the three time-points is shown as an embedded small panel at the upper right of each micrograph (Fig. 10A–I, bar = 2 mm). At high magnification, there was a clear boundary (dotted lines) between the implant and bone in the HAA1 group at 1 month (Fig. 10A) and in the HA group at 1 (Figs. 10G), 3 (Fig. 10H) and 6 months (Fig. 10I). There was no clear boundary between the implant and bone in the HAA1 group at 2 months (Fig. 10B) or 3 months (Fig. 10C), nor in the HAA at 1 (Figs. 10D), 2 (Fig. 10E) or 3 (Fig. 10F) months, where the implanted materials could be seen to be fully integrated with new bone.

It was very difficult to distinguish cells from graft materials on the greyscale SEM/backscatter images (Fig. 10J). However, by using colour coded EDS analysis of Ca, P, N and U, the cell/material interactions could be more clearly observed, with calcium phosphate and calcium carbonate present in different patches. It appears that calcium carbonate particles were surrounded by cells, and left gaps for cells to penetrate into the HAA implants (Fig. 10K).

4. Discussion

New animal models to enable rapid evaluation of the osteogenic potential of biomaterials *in vivo* are highly desirable, as currently-used animal models frequently involve long experimental time courses, increasing costs, as well as painful procedures potentially causing animal suffering, as well as the possibility of infection. In this study we have devised a reliable murine model for rapid assessment of the impacts of biomaterials on bone formation, which involves an easy surgical operation and causes only very mild suffering to the experimental animals. In this model, significantly more bone formation is observed in implanted groups compared with sham-operated controls at 14 days, with 4–8-fold increases in both thickness of the tibial bone and volume of new callus, and new cortical bone formation at 28 days. This model is particularly suitable for rapid initial screening of large numbers of materials within a relatively short period, before more traditional methods for regulatory assessment are perhaps used at later stages. This novel method of rapid biomaterial assessment is likely to reduce the numbers of biomaterials going forward for screening and further significantly reduce the number of experimental animals used.

The new bone formation observed using this model was structurally and compositionally normal. Both osteoblasts and osteoclasts were seen during new bone formation. Intramembranous ossification of trabecular callus between the biomaterial and the bone dominated the bone formation at 14 days after implantation; with the callus being remodelled by osteoclasts to form a new layer of cortical bone by 28 days. The double layer of cortical bone in the tibia appears to be a unique feature which has not been reported before after biomaterial implantation, apart from in cases involving periosteal reaction due to a variety of conditions [36,37].

Interestingly, new bone formation was observed only between the HAA scaffold and the tibial bone, not between the HAA and the anterior tibialis muscle. Bone formation within muscle tissue is typically non-

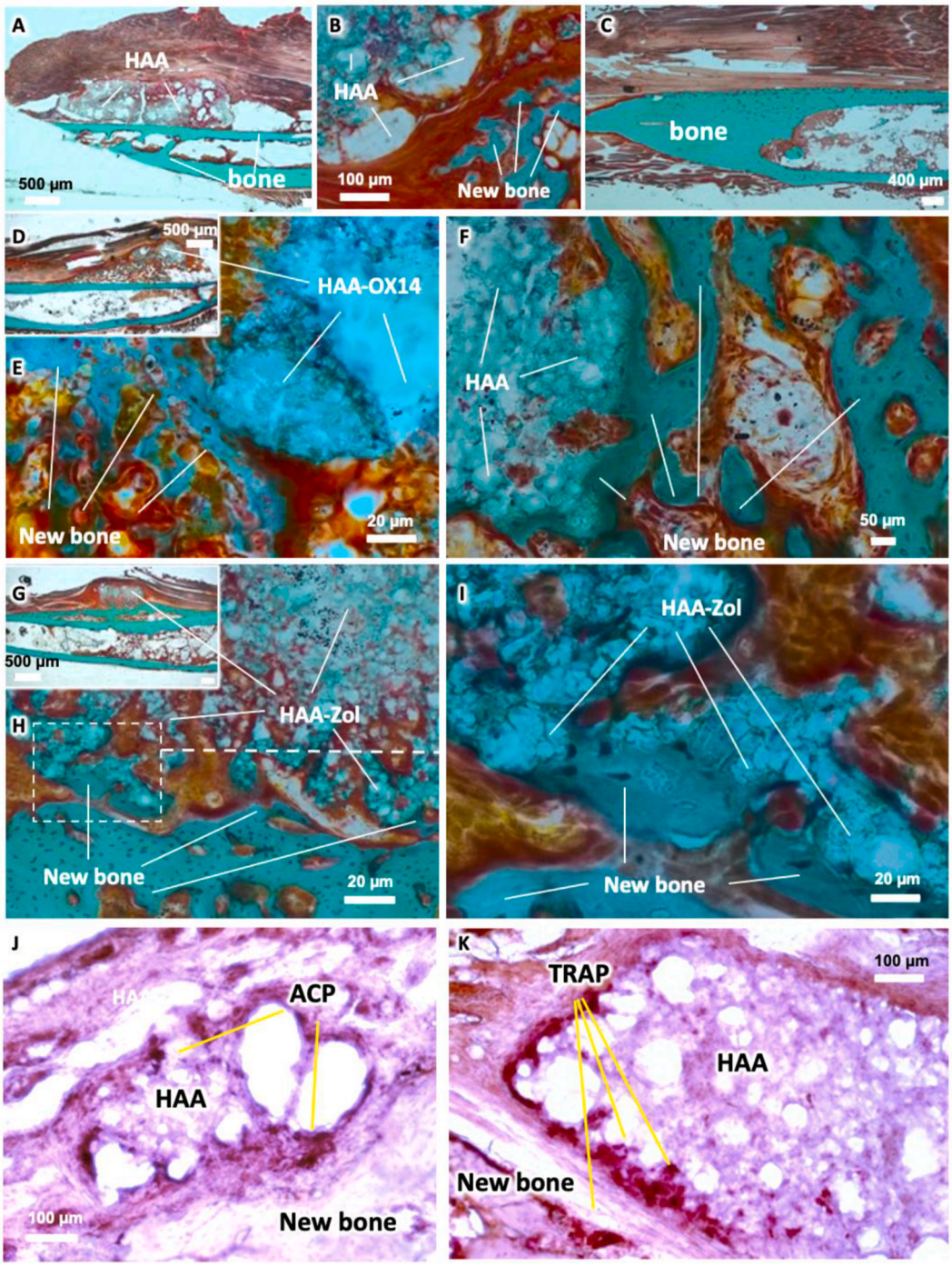

Fig. 6. The Masson-Goldner trichrome and tartrate-resistant acid phosphatase (TRAP) staining of tissue sections after HAA implantation. A. Day 1 after HAA implantation, HAA is in contact with the tibia. **B.** Fourteen days after HAA implantation, new bone formation can be seen near HAA implants. **C.** At 14 days in the sham implantation group, a mild periosteal reactive bone formation can be observed on the tibial surface. **D.** At 14 days after implantation in the OX14 group, large callus formation can be seen between HAA and tibia, showing a nearly four-fold increase in tibial thickness. **E.** Intramembranous ossification between tibia and HAA. **F.** New bone directly formed on the HAA particles. **G.** At 28 days after implantation in the ZOL group, formation of a double layer of cortical bone was observed on the surface of the callus. **H, I.** New blood vessel invade the HAA with bone formation visible on HAA particles. **J.** Acid phosphatase (ACP) without tartrate histochemical staining, ACP-positive cells can be seen surrounding the HAA implants. **K.** TRAP histochemical staining, TRAP-positive osteoclasts are mainly present near the new bone surface.

physiological and requires the presence of morphogens, such as bone morphogenetic proteins, to induce ectopic bone formation [13,15]. As no growth factors were incorporated into the HAA scaffold, only orthotopic bone formation was observed in this study.

There are two types of bone formation involved in healing after long bone injury: intramembranous ossification and endochondral ossification. During endochondral ossification, bone progenitors first form cartilage under low oxygen/poorly angiogenic conditions. After cartilage formation, the cartilage becomes calcified and is then remodelled by osteoclast resorption followed by osteoblasts that form bone around a cartilaginous template [38].

Intramembranous ossification is the process whereby

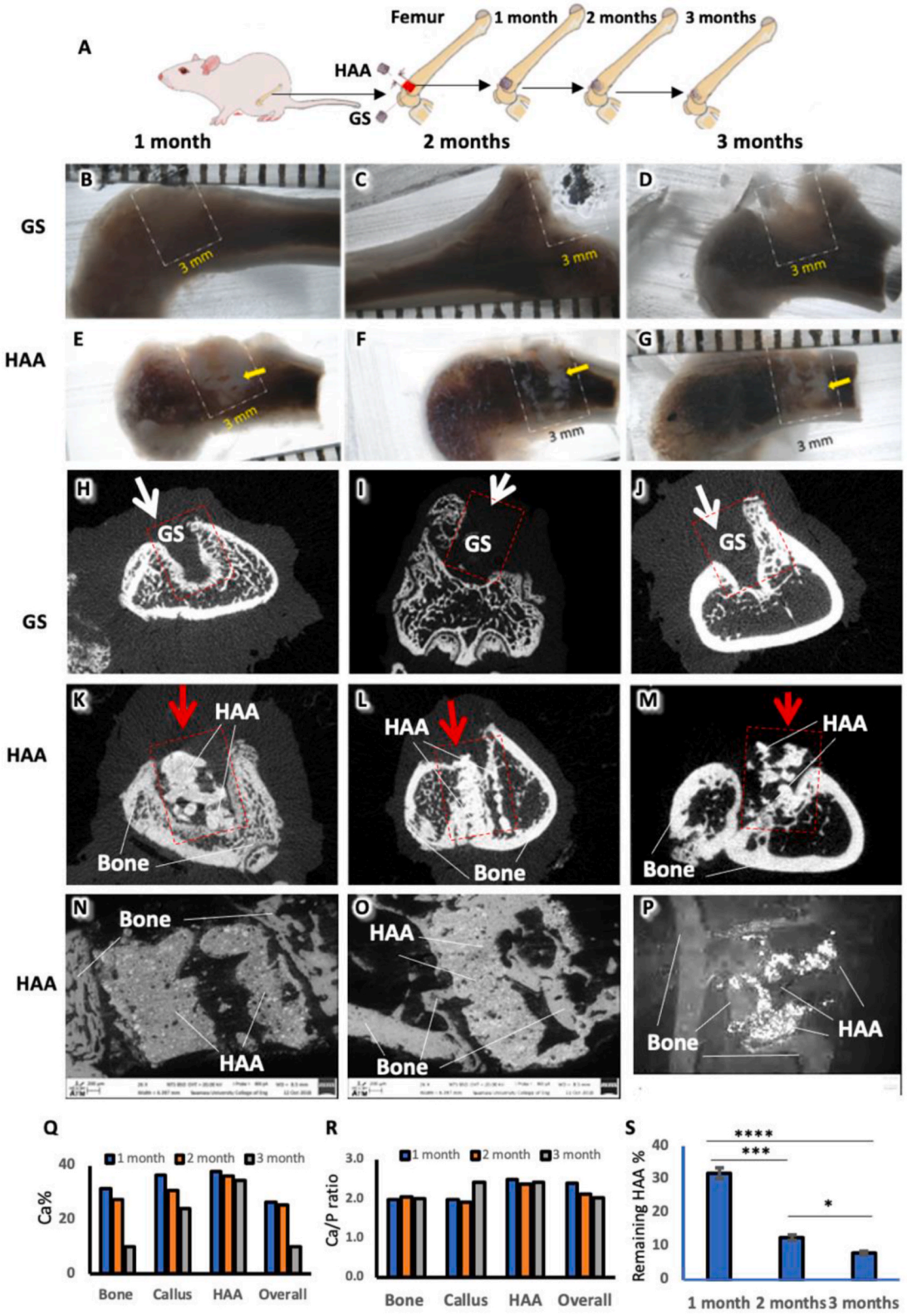

Fig. 7. Assessment of HAA bone regeneration in a 3.5 mm femoral intercondylar critical-size bone defect in SD rats. A. Time-line of the experiment. **B–D.** Gross observation showed that in the control group, the bone defects did not heal, with collapse in structure over 3 months. **E–G.** HAA implants provided structural support and promoted bone regeneration. **H–J.** MicroCT scan of control; and **K–M.** HAA implants over 3 months after implantation. **N–P.** The osteogenesis and biodegradation of HAA after implantation was further observed by SEM/backscatter. The HAA implants showed the presence of electron-dense particles, whereas bone appeared as a more unified tissue. There was a gap between bone and HAA at 1 month (**N**), but the gap was filled with new bone at 2 months while the HAA material was degraded to give space for new bone formation (**O**). At 3 months, most HAA implants were degraded, while new bone was formed and fully integrated into the HAA implants (**P**). **Q, R.** EDS element analysis showed the implants were a mixture of calcium, phosphate with high calcium (Ca) and calcium/phosphate ratio (Ca/P) in HAA implants. **S.** HAA implants in the tissues showed significant decreases in area over three months, showing appreciable biodegradation.

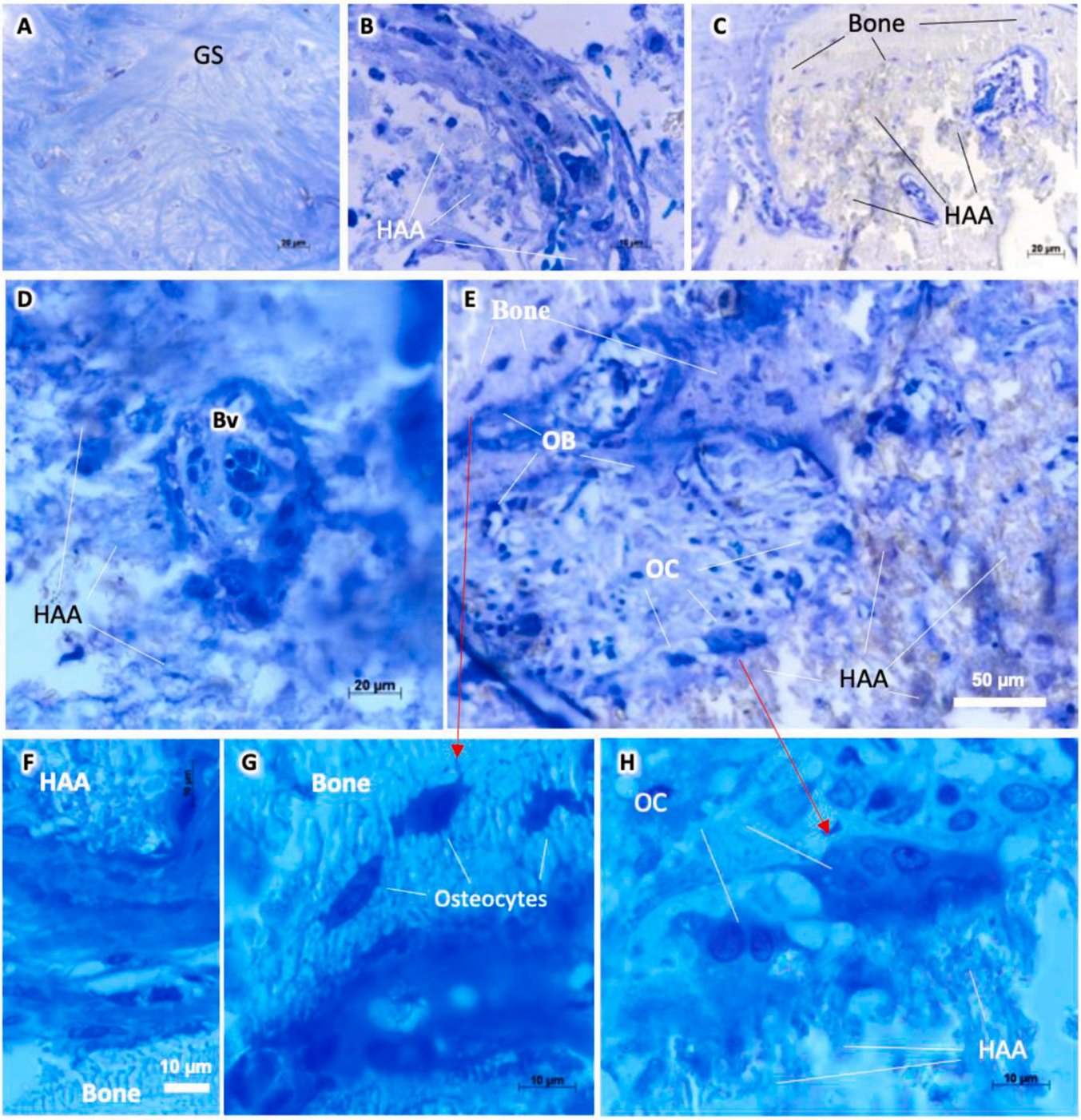

Fig. 8. Light micrographs of non-decalcified sections and toluidine blue staining of HAA and control implants after implantation into 3.5 mm femoral intercondylar defects. Cells are stained as dark blue, bone/fibrous tissues are stained as light blue with osteocytes within lacunae. HAA does not stain and remains as irregular grey patches. **A.** Control group with gelatine sponge (GS) implantation over 3 months showing fibrous tissue without bone formation. **B.** One month after HAA implantation showing fibrous tissue infiltration into the implants. **C.** Two months after HAA implantation, showing bone tissue formation on the surface of HAA. **D.** New blood vessel (Bv) infiltrating into the core of HAA implants at 2 months. **E.** Osteogenesis on HAA at 3 months, where HAA is being removed by osteoclasts (OC) following bone formation by osteoblasts (OB). **F.** Interface between bone and HAA, note osteoblasts on both surfaces. **G.** osteoblasts and osteocytes in newly-formed bone at the frontier of the HAA shown in (**E**). **H.** Two osteoclasts (OC) shown resorbing HAA.

osteoprogenitors form bone directly without the involvement of chondrocytes and calcified cartilage. This bone is normally formed at sites under stable mechanical loading with an adequate oxygenated blood supply [39].

Toluidine blue stains cartilage proteoglycans and glycosaminoglycans pink or purple, but bone tissue is stained blue. In toluidine blue-stained histological sections, no cartilage was observed over the period of HAA implantation in this study. This provides further evidence that the osteogenesis in this rapid bone formation model occurs solely via intramembranous rather than endochondral ossification.

The same HAA biomaterials as used in the mouse study were also implanted into bone defects in rats and minipigs to assess their bone

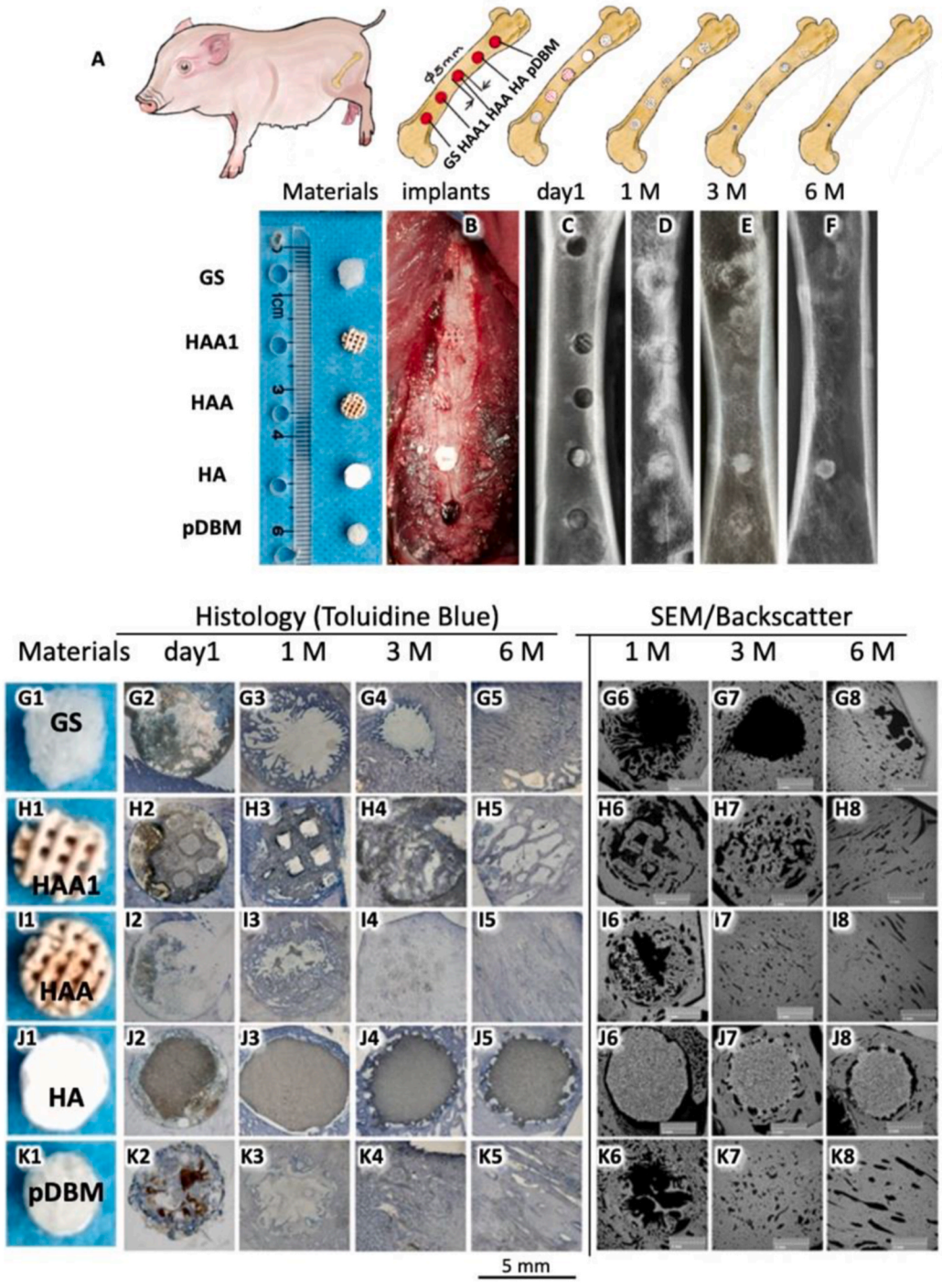

Fig. 9. HAA enhances *in vivo* femoral cortical bone defect regeneration in BAMA minipigs. A. Implantation of five bone graft materials, gelatine sponge (GS); HAA1; HAA2; HA, or pDBM, into 5 mm femoral cortical bone defects in BAMA minipigs. **B.** Surgical implantation of the different graft materials at day 0. **C.** X-ray images of the five implants at 1 day; **D.** 1 month; **E.** 3 months; and **F.** 6 months. **G–K**, Analysis of the grafts. **G1–K1**. The five graft materials before implantation; photomicrographs of the implants stained using Toluidine blue at 1 day after implantation (**G2–K2**), 1 month (**G3–K3**), 3 months (**G4–K4**) and 6 months (**G5–K5**). SEM/backscatter micrographs of the five materials after implantation at 1 month (**G6–K6**) 3 months (**G7–K7**) and 6 months (**G8–K8**) (bar = 5 mm).

formation potential in different species with consistent results, signifying the consistency and reproducibility of the models developed.

It is arguable that animal models may not be necessary for osteogenic assessment, since there are *in vitro* cell culture models, as well as *in vitro* tissue engineering and organ-on-chip methods available. The 3-Rs policy (reduction, refinement, and replacement) is enforced in the UK and other parts of the world to strictly control animal procedures. However, it is unlikely that animal experiments can be completely phased out for the reasons outlined below.

Firstly, *in vivo* assessment is compulsory to meet governmental regulatory control of implantable biomaterials to evaluate their biocompatibility and efficacy. Secondly, bone formation in the clinical situation requires angiogenesis, innervation, osteoblastic bone formation and osteoclastic bone resorption which mandates an *in vivo* model as no *in vitro* model can yet reproduce the necessary complexity of tissue interactions. Multiple genetic events and molecular cascades are involved,

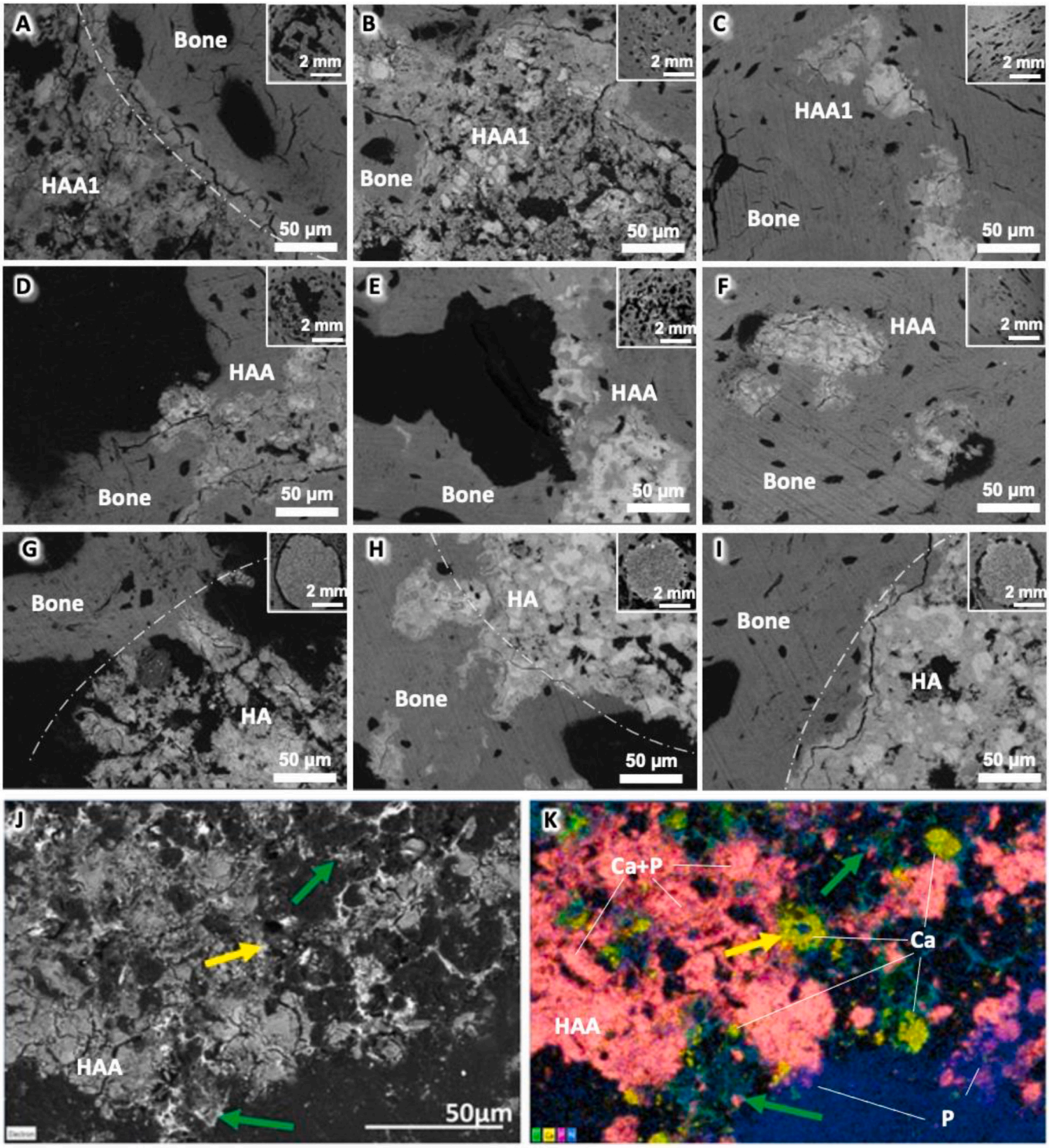

Fig. 10. SEM/backscatter micrographs and colour-coded EDS analysis. A–I. The interface between the implants (HAA1, HAA2 and HA) and bone at 1, 3 and 6 months. The overall surface structure of each material at each of the three time-points is shown as an embedded small picture at the upper right of each micrograph (**A–I**, bar = 2 mm). There was a clear boundary (dotted lines) between implant and bone in the HAA1 group at 1-month (**A**) and in the HA group at 1 (**G**), 3 (**H**) and 6 (**I**) months. There was no clear boundary between implants and bone in the HAA1 group at 2 (**B**) or 3 (**C**) months, nor in the HAA group at 1 (**D**), 2 (**E**) or 3 (**F**) months, where the implanted materials were fully integrated with new bone. Micrographs of SEM/backscatter without EDS (**J**) and with EDS (**K**) analysis are shown. **J.** it is very difficult to distinguish cells from materials on the greyscale electron image of SEM/backscatter observations. **K.** Using colour-coded EDS analysis of Ca, P, N and U, the cell/material interaction can be detected as: bulk calcium phosphate (Ca + P), orange; calcium (Ca, carbonate) fragments, yellow; (hydrogen) phosphate (P), purple; cells/extracellular matrix (blue or/and green).

and this environment is not reproducible in a test tube. Thirdly, it is well known that bone remodelling needs mechanical stimulation under physiological conditions. Finally, the biodegradation and the products of biomaterial degradation may cause inflammatory responses involving immune cells. These conditions only exist in the living body. Since animal testing is inevitable in implantable biomaterial development, the best approach will be the application of the 3R rules.

We believe that the animal models we developed in this study meet the 3R principle very well. Since the procedure does not involve fracture or bone defects and the bone formation tested is highly reproducible and reliable, it significantly reduces animal suffering, while also reducing the time and resources needed. This model is a refinement of previously-used fracture healing and bone defect regeneration models. Even though bone fracture and defect models may still be needed for final regulatory tests, at least the initial tests may be replaced by our refined and reduced method.

HAA scaffolds were used as test biomaterials for osteogenesis assessment in this study. HAA is made up of hydroxyapatite and calcium carbonate, and characterisation by FTIR confirmed the findings of previous investigators [27,40]. Although hydroxyapatite is a widely-used bone graft material, there are a number of drawbacks with its use, including slow resorption rate, poor osteointegration and limited bioactivities. To increase the resorption of hydroxyapatite, it is frequently used in combination with beta-calcium phosphate to form biphasic ceramic bone grafts [41]. However, both hydroxyapatite and beta-calcium phosphate ceramics are different from natural bone, due to differences in their physicochemical properties, for example, stoichiometry, crystallinity, and solubility [42]. Calcium phosphate ceramics may induce cellular inflammatory responses, due to the release of ceramic particles after material degradation [42,43].

For bone grafts it is highly desirable for any potential biomaterial to have a composition as similar as possible to that of natural bone mineral, that better supports bone formation and is fully biodegradable. Previous studies have shown that biomaterials combining hydroxyapatite and calcium phosphate, for example, incompletely converted coralline hydroxyapatite, are highly osteogenic and are also fully biodegradable after bone regeneration [44–46]. Based on this finding, a 3D-printed biomaterial, HAA consisting of hydroxyapatite and calcium carbonate, was used for testing in this animal model [27].

This rapid periosteal bone formation model is a quantifiable and highly-reproducible model for osteogenic assessment of biomaterials. However, as mentioned above, the effect of the biomaterial on fracture healing/bone regeneration must be confirmed by implanting the biomaterials into bone defect sites in both small and large animals. It is apparent that HAA only forms bone at orthotopic sites between the tibial periosteum and HAA implants and there is no ectopic bone formation at the HAA/muscle interface.

To validate the osteogenic capacity of HAA in bone defects, trabecular bone defects in rat femoral condyle and cortical bone defects in the BAMA minipig femur were further assessed. Rapid bone regeneration of HAA over 1–3 months and complete biodegradation within 6 months after bone regeneration were confirmed.

The mechanism of rapid bone formation and full biodegradation of HAA was not fully investigated in this study. Since no growth factors nor pharmaceutical ingredients were added during the production of HAA, we propose that its composition, especially the incorporation of calcium carbonate, may have played a very important role in the biodegradation and osteogenesis of HAA.

Calcium carbonate is a natural mineral component of non-vertebrae life-forms such as shellfish and coral, and it has long been recognised as an important mineral for mammalian bone formation as well [47,48]. In bone apatite, calcium can be replaced by magnesium (up to 8.5 %) or strontium (up to 20 %), and HPO_4^{2-} ions can be exchanged by carbonate (up to 44 %) [48].

Calcium carbonate is more soluble than hydroxyapatite. In our study, calcium carbonate may be dissolved first, thus leaving channels or pockets for ingrowth of bone cells which subsequently form bone tissue. This is consistent with a previous study showing that calcium carbonate was biodegraded by the enzyme carbonic anhydrase, which caused local dissolution and created space for newly-synthesised bone tissue [49]. This may explain the more rapid bone formation and also faster biodegradation of HAA in comparison with implantation of HA alone. However, further study is needed to confirm whether or not calcium carbonate contributes to this process.

SEM/EDS methods are traditionally used in materials and geological sciences research, but have become a rapidly-developing area for biological study [50,51]. The Ultim Extreme system is specifically designed for high analytical sensitivity of elements with low atomic number and is thus ideal for the detection of nitrogen and oxygen in biological specimens in addition to inorganic chemicals such as metals and minerals. With increased sensitivity and quantitative potential it is expected that this technique will become more broadly applicable to study tissue/-biomaterials interfaces.

To demonstrate the quantitative differences in new bone formation of this model, we used local delivery of two bisphosphonates, OX14 and zoledronate, to assess whether they might reduce bone remodelling and retain more callus. Larger quantities of callus are expected to be beneficial in the early stage of bone healing, though the exact amount varies between bisphosphonates [33,52,53]. OX14 is a novel bisphosphonate which has high potency but low mineral affinity in comparison with other bisphosphonates [54] due to the -OH side chain replacement by -F, but which has similar high potency to inhibit osteoclast bone resorption activity. Interestingly, in this study, only zoledronate demonstrated significantly more callus formation at 28 days post-implantation. This effect appears likely to depend on the affinity of binding of the bisphosphonate to the calcium phosphate biomaterial and the retention of bisphosphonate at the site of biomaterial dissolution and bone formation. This is evidenced by the distinction between the observed effect of the high mineral affinity zoledronate compared with that of the low mineral binding OX14.

However, while the inclusion of OX14 did not have any effect during this study, only one concentration was tested *in vivo* and a higher concentration may have comparable effects to zoledronate. Additionally, the lower binding capacity of OX14 could mean that less OX14 than expected may be attached to the scaffolds during the soaking step. The inability to directly add bisphosphonates to HAA scaffolds during production, as well as the difficulty of measuring extremely low concentrations of bisphosphonates, made this more challenging to assess. Nevertheless, this observation highlights the potential of bisphosphonates as an addition to bone scaffolds for the purpose of enhancing the bone healing process.

There are some limitations of this study. Firstly, this is probably the first murine periosteal bone formation model used to evaluate the osteogenic capacity of biomaterials. Therefore, more experimental data are needed before this model can be accepted as a standard model for bone formation assessment and comparison. Secondly, the cells involved in such rapid bone formation need to be identified further to determine whether or not they are periosteal stem cells. Thirdly, small animals have better ability to form bone than large mammals and humans during bone regeneration. This model is only suitable for the screening of large numbers of different biomaterials for their osteogenic potential. Large animal tests and clinical trials are still needed before any clinical application. Finally, microCT appears to be the most reliable quantitative method for callus size measurement; however, the commercial software to quantify the bone parameters are not suitable for biomaterial evaluation. New methods are desirable for this purpose.

5. Conclusion

This study has shown that the mouse tibial periosteal intramembranous ossification model is an excellent model for comparison of the osteogenic potentials of bone scaffolds, as calluses are reliably

produced and vary in size depending on the scaffold composition. Additionally, it demonstrates that calcium carbonate enhances biodegradation and osteogenesis in combination with hydroxyapatite. These findings will significantly contribute to future research in bioactive material development for bone regeneration.

CRediT authorship contribution statement

Emma Steijvers: Writing – original draft, Visualization, Methodology, Investigation, Formal analysis, Data curation. **Yunshong Shi:** Writing – original draft, Visualization, Validation, Methodology, Investigation, Formal analysis, Data curation. **Hong Lu:** Investigation, Formal analysis, Data curation. **Weixin Zhang:** Visualization, Validation, Methodology, Investigation, Formal analysis, Data curation. **Yitian Zhang:** Writing – original draft, Visualization, Formal analysis, Data curation. **Feihu Zhao:** Visualization, Supervision, Formal analysis, Data curation. **Baichuan Wang:** Supervision, Resources, Methodology, Data curation, Conceptualization. **Louise Hughes:** Visualization, Resources, Formal analysis, Data curation, Conceptualization. **Jake E. Barralet:** Resources, Funding acquisition, Conceptualization. **Giulia Degli-Alessandrini:** Writing – original draft, Visualization, Resources, Formal analysis, Data curation. **Igor Kraev:** Visualization, Methodology, Investigation. **Richard Johnston:** Visualization, Methodology, Data curation. **Zengwu Shao:** Validation, Resources, Investigation, Conceptualization. **Frank H. Ebetino:** Writing – original draft, Validation, Resources, Methodology. **James T. Triffitt:** Writing – original draft, Validation, Resources, Conceptualization. **R. Graham G. Russell:** Writing – review & editing, Validation, Resources, Methodology, Conceptualization. **Davide Deganello:** Writing – review & editing, Validation, Supervision, Resources, Methodology, Funding acquisition, Conceptualization. **Xu Cao:** Validation, Supervision, Resources, Funding acquisition, Conceptualization. **Zhidao Xia:** Writing – review & editing, Writing – original draft, Visualization, Validation, Supervision, Resources, Project administration, Methodology, Investigation, Funding acquisition, Formal analysis, Data curation, Conceptualization.

Declaration of competing interest

The authors declare no competing financial interests.

Ethics approval and consent to participate

1. The animal protocols for mouse related work were approved by the Institutional Animal Care and Use Committee of Johns Hopkins University, Baltimore, MD, USA (MO21M276).
2. The work on rats and minipigs were approved by the Institutional Animal Care and Use Committee (IACUC Number 738, Tongji Medical School, Huazhong University of Science and Technology)

Acknowledgements

This project was supported by Royal Society International Exchanges Grant 2021 (IES\R1\211128), Québec–Wales Collaboration Grant 2021 and Wales Innovation Network (WIN) Small Grants Fund (SG6-RIR1058-107). We would like to thank Prof. Cathy Thornton and Dr Ruth Jones for providing human umbilical cords, and Dr Christopher Von Ruhland, CBS, Cardiff University for supporting the resin embedding and sampling process.

Appendix A. Supplementary data

Supplementary data to this article can be found online at https://doi.org/10.1016/j.bioactmat.2024.11.025.

References

[1] A. Salhotra, H.N. Shah, B. Levi, M.T. Longaker, Mechanisms of bone development and repair, Nat. Rev. Mol. Cell Biol. 21 (11) (2020) 696–711.
[2] E.E. Huang, N. Zhang, H. Shen, X. Li, M. Maruyama, T. Utsunomiya, Q. Gao, R. A. Guzman, S.B. Goodman, Novel techniques and future perspective for investigating critical-size bone defects, Bioengineering 9 (4) (2022).
[3] G.N. Duda, S. Geissler, S. Checa, S. Tsitsilonis, A. Petersen, K. Schmidt-Bleek, The decisive early phase of bone regeneration, Nat. Rev. Rheumatol. 19 (2) (2023) 78–95.
[4] G. Battafarano, M. Rossi, V. De Martino, F. Marampon, L. Borro, A. Secinaro, A. Del Fattore, Strategies for bone regeneration: from graft to tissue engineering, Int. J. Mol. Sci. 22 (3) (2021).
[5] J.M. Sadowska, M. Ziminska, C. Ferreira, A. Matheson, A. Balouch, J. Bogle, S. Wojda, J. Redmond, A. Elkashif, N. Dunne, H.O. McCarthy, S. Donahue, F. J. O'Brien, Development of miR-26a-activated scaffold to promote healing of critical-sized bone defects through angiogenic and osteogenic mechanisms, Biomaterials 303 (2023) 122398.
[6] D. Buser, I. Urban, A. Monje, M.F. Kunrath, C. Dahlin, Guided bone regeneration in implant dentistry: basic principle, progress over 35 years, and recent research activities, Periodontol 93 (1) (2000) 9–25, 2023.
[7] N. Donos, A. Akcali, N. Padhye, A. Sculean, E. Calciolari, Bone regeneration in implant dentistry: which are the factors affecting the clinical outcome? Periodontol 93 (1) (2000) 26–55, 2023.
[8] A. Szwed-Georgiou, P. Plocinski, B. Kupikowska-Stobba, M.M. Urbaniak, P. Rusek-Wala, K. Szustakiewicz, P. Piszko, A. Krupa, M. Biernat, M. Gazinska, M. Kasprzak, K. Nawrotek, N.P. Mira, K. Rudnicka, Bioactive materials for bone regeneration: biomolecules and delivery systems, ACS Biomater. Sci. Eng. 9 (9) (2023) 5222–5254.
[9] T.F. Moriarty, L.G. Harris, R.A. Mooney, J.C. Wenke, M. Riool, S.A.J. Zaat, A. Moter, T.P. Schaer, N. Khanna, R. Kuehl, V. Alt, A. Montali, J. Liu, S. Zeiter, H. J. Busscher, D.W. Grainger, R.G. Richards, Recommendations for design and conduct of preclinical in vivo studies of orthopedic device-related infection, J. Orthop. Res. 37 (2) (2019) 271–287.
[10] H. Wang, J.A. Chediak, P.J. Belmont, D.M. Saylor, K.S. Phillips, Preclinical performance testing of medical devices with antimicrobial effects, Nat. Rev. Bioeng. 1 (8) (2023) 589–605.
[11] A. Bigham-Sadegh, A. Oryan, Selection of animal models for pre-clinical strategies in evaluating the fracture healing, bone graft substitutes and bone tissue regeneration and engineering, Connect. Tissue Res. 56 (3) (2015) 175–194.
[12] M. Peric, I. Dumic-Cule, D. Grcevic, M. Matijasic, D. Verbanac, R. Paul, L. Grgurevic, V. Trkulja, C.M. Bagi, S. Vukicevic, The rational use of animal models in the evaluation of novel bone regenerative therapies, Bone 70 (2015) 73–86.
[13] M.A. Scott, B. Levi, A. Askarinam, A. Nguyen, T. Rackohn, K. Ting, C. Soo, A. W. James, Brief review of models of ectopic bone formation, Stem Cell. Dev. 21 (5) (2012) 655–667.
[14] T. Taguchi, M.J. Lopez, An overview of de novo bone generation in animal models, J. Orthop. Res. 39 (1) (2021) 7–21.
[15] K. Hashimoto, T. Kaito, M. Furuya, S. Seno, D. Okuzaki, J. Kikuta, H. Tsukazaki, H. Matsuda, H. Yoshikawa, M. Ishii, In vivo dynamic analysis of BMP-2-induced ectopic bone formation, Sci. Rep. 10 (1) (2020) 4751.
[16] M.A. Scott, B. Levi, A. Askarinam, A. Nguyen, T. Rackohn, K. Ting, C. Soo, A. W. James, Brief review of models of ectopic bone formation, Stem Cell. Dev. 21 (5) (2012) 655–667.
[17] Y. Li, S.K. Chen, L. Li, L. Qin, X.L. Wang, Y.X. Lai, Bone defect animal models for testing efficacy of bone substitute biomaterials, J. Orthop. Translat. 3 (3) (2015) 95–104.
[18] A. Pearce, R. Richards, S. Milz, E. Schneider, S. Pearce, Animal models for implant biomaterial research in bone: a review, Eur. Cell. Mater. 13 (2007) 1–10.
[19] S.L. Piotrowski, L. Wilson, N. Dharmaraj, A. Hamze, A. Clark, R. Tailor, L.R. Hill, S. Lai, F.K. Kasper, S. Young, Development and characterization of a rabbit model of compromised maxillofacial wound healing, Tissue Eng. C Methods 25 (3) (2019) 160–167.
[20] J.P. Schmitz, J.O. Hollinger, The critical size defect as an experimental model for craniomandibulofacial nonunions, Clin. Orthop. Relat. Res. 205 (1986) 299–308.
[21] R.A. Delgado-Ruiz, J.L. Calvo-Guirado, G.E. Romanos, Critical size defects for bone regeneration experiments in rabbit calvariae: systematic review and quality evaluation using ARRIVE guidelines, Clin. Oral Implants Res. 26 (8) (2015) 915–930.
[22] I. Beitlitum, F. Rayyan, A. Pokhojaev, H. Tal, R. Sarig, A novel micro-CT analysis for evaluating the regenerative potential of bone augmentation xenografts in rabbit calvarias, Sci. Rep. 14 (1) (2024) 4321.
[23] O. Duchamp De Lageneste, A. Julien, R. Abou-Khalil, G. Frangi, C. Carvalho, N. Cagnard, C. Cordier, S.J. Conway, C. Colnot, Periosteum contains skeletal stem cells with high bone regenerative potential controlled by Periostin, Nat. Commun. 9 (1) (2018).
[24] B. Gao, R. Deng, Y. Chai, H. Chen, B. Hu, X. Wang, S. Zhu, Y. Cao, S. Ni, M. Wan, L. Yang, Z. Luo, X. Cao, Macrophage-lineage TRAP+ cells recruit periosteum-derived cells for periosteal osteogenesis and regeneration, J. Clin. Invest. 129 (6) (2019) 2578–2594.
[25] N. Zhang, L. Hu, Z. Cao, X. Liu, J. Pan, Periosteal skeletal stem cells and their response to bone injury, Front. Cell Dev. Biol. 10 (2022) 812094.
[26] W. Zhou, S.Q. Ke, Z. Huang, W. Flavahan, X. Fang, J. Paul, L. Wu, A.E. Sloan, R. E. McLendon, X. Li, J.N. Rich, S. Bao, Periostin secreted by glioblastoma stem cells recruits M2 tumour-associated macrophages and promotes malignant growth, Nat. Cell Biol. 17 (2) (2015) 170–182.

[27] Y. Shi, R. He, X. Deng, Z. Shao, D. Deganello, C. Yan, Z. Xia, Three-dimensional biofabrication of an aragonite-enriched self-hardening bone graft substitute and assessment of its osteogenicity in vitro and in vivo, Biomater Transl. 1 (1) (2020) 69–81.
[28] R.G. Russell, Z. Xia, J.E. Dunford, U. Oppermann, A. Kwaasi, P.A. Hulley, K. L. Kavanagh, J.T. Triffitt, M.W. Lundy, R.J. Phipps, B.L. Barnett, F.P. Coxon, M. J. Rogers, N.B. Watts, F.H. Ebetino, Bisphosphonates: an update on mechanisms of action and how these relate to clinical efficacy, Ann. N. Y. Acad. Sci. 1117 (2007) 209–257.
[29] M.A. Lawson, F.H. Ebetino, A. Mazur, A.D. Chantry, J. Paton-Hough, H.R. Evans, D. Lath, M.K. Tsoumpra, M.W. Lundy, R.L. Dobson, M. Quijano, A.A. Kwaasi, J. E. Dunford, X. Duan, J.T. Triffitt, G. Jeans, R.G.G. Russell, The pharmacological profile of a novel highly potent bisphosphonate, OX14 (1-Fluoro-2-(Imidazo-[1,2-alpha]Pyridin-3-yl)-Ethyl-Bisphosphonate), J. Bone Miner. Res. 32 (9) (2017) 1860–1869.
[30] K.L. Kavanagh, K. Guo, J.E. Dunford, X. Wu, S. Knapp, F.H. Ebetino, M.J. Rogers, R. G. Russell, U. Oppermann, The molecular mechanism of nitrogen-containing bisphosphonates as antiosteoporosis drugs, Proc. Natl. Acad. Sci. U. S. A. 103 (20) (2006) 7829–7834.
[31] S. Ray, U. Thormann, M. Eichelroth, M. Budak, C. Biehl, M. Rupp, U. Sommer, T. El Khassawna, F.I. Alagboso, M. Kampschulte, M. Rohnke, A. Henß, K. Peppler, V. Linke, P. Quadbeck, A. Voigt, F. Stenger, D. Karl, R. Schnettler, C. Heiss, K. S. Lips, V. Alt, Strontium and bisphosphonate coated iron foam scaffolds for osteoporotic fracture defect healing, Biomaterials 157 (2018) 1–16.
[32] Z. Yang, W. Chen, Z. Xia, Y. Liu, S. Peggrem, T. Geng, Z. Yang, H. Li, B. Xu, C. Zhang, J.T. Triffitt, Y. Zhang, Local application of ibandronate/gelatin sponge improves osteotomy healing in rabbits, PLoS One 10 (5) (2015) e0125807.
[33] S.L. Kates, C.L. Ackert-Bicknell, How do bisphosphonates affect fracture healing? Injury 47 (1) (2016) S65–S68. Suppl 1(0.
[34] A.G.E. Day, W.R. Francis, K. Fu, I.L. Pieper, O. Guy, Z. Xia, Osteogenic potential of human umbilical cord mesenchymal stem cells on coralline hydroxyapatite/calcium carbonate microparticles, Stem Cell. Int. 2018 (2018) 4258613.
[35] R. Ward-Flanagan, C.T. Dickson, Intravenous chloral hydrate anesthesia provides appropriate analgesia for surgical interventions in male Sprague-Dawley rats, PLoS One 18 (6) (2023) e0286504.
[36] R.S. Rana, J.S. Wu, R.L. Eisenberg, Periosteal reaction, AJR Am. J. Roentgenol. 193 (4) (2009) W259–W272.
[37] C.H. Maia Ferreira Alencar, C.R. Sampaio Silveira, M.M. Cavalcante, C.G. Maia Vieira, M.J. Diogenes Teixeira, F.A. Neto, A. de Abreu, A. Chhabra, Periosteum: an imaging review, Eur. J. Radiol Open 7 (2020) 100249.
[38] G.L. Galea, M.R. Zein, S. Allen, P. Francis-West, Making and shaping endochondral and intramembranous bones, Dev. Dynam. 250 (3) (2021) 414–449.
[39] Y.Q. Yang, Y.Y. Tan, R. Wong, A. Wenden, L.K. Zhang, A.B. Rabie, The role of vascular endothelial growth factor in ossification, Int. J. Oral Sci. 4 (2) (2012) 64–68.
[40] Y. Shi, R. He, X. Deng, Z. Shao, D. Deganello, C. Yan, X. Z, Three-dimensional biofabrication of an aragonite enriched self-hardening bone graft substitute and assessment of its osteogenicity in vitro and in vivo, Biomater. Trans. 1 (1) (2020) 69–81.
[41] J.M. Bouler, P. Pilet, O. Gauthier, E. Verron, Biphasic calcium phosphate ceramics for bone reconstruction: a review of biological response, Acta Biomater. 53 (2017) 1–12.
[42] K. Maruyama, J.Y. Cheng, H. Ishii, Y. Takahashi, V. Zangiacomi, T. Satoh, T. Hosono, K. Yamaguchi, Activation of NLRP3 inflammasome complexes by beta-tricalcium phosphate particles and stimulation of immune cell migration in vivo, J. Innate Immun. 14 (3) (2022) 207–217.
[43] F. Velard, J. Braux, J. Amedee, P. Laquerriere, Inflammatory cell response to calcium phosphate biomaterial particles: an overview, Acta Biomater. 9 (2) (2013) 4956–4963.
[44] K. Fu, Q. Xu, J. Czernuszka, J.T. Triffitt, Z. Xia, Characterization of a biodegradable coralline hydroxyapatite/calcium carbonate composite and its clinical implementation, Biomed. Mater. 8 (6) (2013) 065007.
[45] K. Fu, Q. Xu, J. Czernuszka, C.E. McKenna, F.H. Ebetino, R.G. Russell, J.T. Triffitt, Z. Xia, Prolonged osteogenesis from human mesenchymal stem cells implanted in immunodeficient mice by using coralline hydroxyapatite incorporating rhBMP2 microspheres, J. Biomed. Mater. Res. 92 (4) (2010) 1256–1264.
[46] J. Laine, M. Labady, A. Albornoz, S. Yunes, Porosities and pore sizes in coralline calcium carbonate, Mater. Char. 59 (10) (2008) 1522–1525.
[47] R.M. Biltz, E.D. Pellegrino, The nature of bone carbonate, Clin. Orthop. Relat. Res. 129 (1977) 279–292.
[48] C. Rey, C. Combes, C. Drouet, M.J. Glimcher, Bone mineral: update on chemical composition and structure, Osteoporos. Int. 20 (6) (2009) 1013–1021.
[49] C. Rey, C. Combes, C. Drouet, D. Grossin, G. Bertrand, J. Soulié, 1.11 bioactive calcium phosphate compounds: physical chemistry, in: P. Ducheyne (Ed.), Comprehensive Biomaterials II, Elsevier, Oxford, 2017, pp. 244–290.
[50] L. Hughes, R. Vowden, Z. Xia, Multi-colour electron microscopy: protein accumulation and cellular activity surrounding hydroxyapatite implants revealed by energy dispersive X-ray spectrometry, Microsc. Microanal. 26 (S2) (2020) 1346–1347.
[51] J.L.P. Machado, L. Hughes, Z. Xia, Correlative Raman, backscattered electron and X-ray imaging and energy dispersive X-ray spectrometry uncovers unique chemical signatures surrounding nanoparticles and wear debris in periprosthetic tissue, Microsc. Microanal. 30 (1) (2024) 2124–2125.
[52] L.J. Kidd, N.R. Cowling, A.C. Wu, W.L. Kelly, M.R. Forwood, Bisphosphonate treatment delays stress fracture remodeling in the rat ulna, J. Orthop. Res. 29 (12) (2011) 1827–1833.
[53] J. Li, S. Mori, Y. Kaji, T. Mashiba, J. Kawanishi, H. Norimatsu, Effect of bisphosphonate (incadronate) on fracture healing of long bones in rats, J. Bone Miner. Res. 14 (6) (1999) 969–979.
[54] M.A. Lawson, F.H. Ebetino, A. Mazur, A.D. Chantry, J. Paton-Hough, H.R. Evans, D. Lath, M.K. Tsoumpra, M.W. Lundy, R.L. Dobson, M. Quijano, A.A. Kwaasi, J. E. Dunford, X. Duan, J.T. Triffitt, G. Jeans, R.G.G. Russell, The pharmacological profile of a novel highly potent bisphosphonate, OX14 (1-Fluoro-2-(Imidazo-[1,2-α]Pyridin-3-yl)-Ethyl-Bisphosphonate), J. Bone Miner. Res. 32 (9) (2017) 1860–1869.